CELL BIOLOGY

Genetics- and age-driven neuroimmune and disc changes underscore herniation susceptibility and pain-associated behaviors in SM/J mice

Emanuel J. Novais[1,2,3,4]†, Olivia K. Ottone[2,5]†, Eric V. Brown[6], Vedavathi Madhu[2], Victoria A. Tran[2], Pranay Ramteke[2], Abhijit S. Dighe[7,8], Michael D. Solga[9], Alexandra Manchel[5], Angelo C. Lepore[6], Makarand V. Risbud[2,5]*

There are no appropriate mouse models to study the pathophysiology of spontaneous disc herniations in a wild-type setting. SM/J mice, a poor healer inbred strain, presented a high incidence of age-associated lumbar disc herniations with neurovascular innervations. Transcriptomic comparisons of the SM/J annulus fibrosus with human tissues showed shared pathways related to immune cell activation and inflammation. Notably, aged SM/J mice showed increased pain sensitization and neuroinflammation with altered extracellular matrix regulation in the dorsal root ganglia and spinal cord. There were increased T cells in the vertebral marrow, and cytometry by time-of-flight analysis showed increased splenic CD8+ T cells, nonspecific activation of CD8+ memory T cells, and enhanced interferon-γ production in the myeloid compartment. Single-cell RNA sequencing of peripheral blood mononuclear cells showed more B cells, with lower proportions of T cells, monocytes, and granulocytes. This study highlights the contribution of genetic background and aging to increased susceptibility of spontaneous intervertebral disc herniations in a clinically relevant murine model.

INTRODUCTION

With increased human lifespan, the interest in understanding age-dependent diseases has grown (*1*). Musculoskeletal diseases, including osteoarthritis, osteoporosis, and intervertebral disc degeneration, are associated with aging, chronic pain, loss of mobility, and disability (*1*). Disc degeneration is one of the major contributors to chronic low back pain (cLBP), a leading cause of years lived with disability (*2*).

While disc pathology manifests as a host of phenotypes, including fibrosis, calcification, and herniation (*3*), understanding each is hampered by the lack of appropriate animal models. Although mouse models are developed to understand these degenerative phenotypes (*4*–*6*), studies of herniation are limited to injury models that capture local changes after acute herniations but fail to recapitulate age-related chronic changes (*7*). Similarly, while transgenic and knockout mice have shown increased susceptibility to spontaneous herniations (*8*, *9*) and corresponding immune changes, they have limited translatability to humans because of single gene contributions and other comorbidities (*10*). Notably, 85% of symptomatic human disc herniations are resorbed within 6 weeks because of neutrophil/macrophage and immune cell recruitment by the local pro-inflammatory and chemotactic signals (*11*). Recent studies indicate that inhibiting these early inflammatory processes delays resorption and causes a transition to a chronic pain state (*12*, *13*).

Many degenerative pathologies associated with chronic pain show increased innervation related to local expression of nerve growth factor (NGF) and protein gene product 9.5 (*14*, *15*). Notably, markers such as calcitonin gene-related peptide (CGRP) and isolectin B4 (IB4) are used to discern peptidergic and nonpeptidergic nociceptive neurons (*16*). While discs, facet joints, muscle, ligament, and fascia all can contribute to back pain, the sensory information is transmitted through identical circuits: local peripherical nociceptive neurons in dorsal root ganglia (DRG), the dorsal horn in the spinal cord, and lastly, the specific sensory brain region (*17*). Furthermore, immune and glial activation in the central and peripheral nervous systems is thought to mediate the transition from acute to chronic pain (*18*).

In the present study, we provide comprehensive analyses of the pathophysiology and interdependence of spontaneous lumbar disc herniations and radiculopathy in SM/J mice, which we found are highly susceptible to age-dependent herniation pathology (*19*). SM/J, a poor healer mouse strain, has become an attractive model for studying spontaneous disc degeneration because of the early onset of pathology in the caudal spine (*19*, *20*). These mice have a comparable lifespan to the commonly used C57BL/6 strain, and disc degeneration is not the result of a single gene mutation or external injury (*4*). A similar degeneration process is also observed in genetically susceptible human populations, as suggested by twin studies (*21*). Broadly, our studies highlight the strong association between immune system dysregulation in chronic pain because of disc herniation and emphasize the importance of genetic background to the susceptibility of age-associated herniations.

RESULTS

SM/J mice show a high incidence of age-associated lumbar disc herniations

We characterized the lumbar spinal phenotype of SM/J mice at 6, 12, and 20 months (M) and compared it to age-matched C57BL/6 mice.

[1]Orthopaedic Department, Local Health Unit of the Litoral Alentejano, Santiago do Cacém, Portugal. [2]Department of Orthopaedic Surgery, Sidney Kimmel Medical College, Thomas Jefferson University, Philadelphia, PA, USA. [3]Faculty of Medicine, Universidade Católica Portuguesa, Lisbon, Portugal. [4]Center for Interdisciplinary Research in Health, Universidade Católica Portuguesa, Lisbon, Portugal. [5]Graduate Program in Cell Biology and Regenerative Medicine, Jefferson College of Life Sciences, Thomas Jefferson University, Philadelphia, PA, USA. [6]Department of Neuroscience, Vickie and Jack Farber Institute for Neuroscience, Sidney Kimmel Medical College at Thomas Jefferson University, Philadelphia, PA, USA. [7]Department of Orthopedic Surgery, University of Virginia Health System, Charlottesville, VA, USA. [8]Center for Public Health Genomics, University of Virginia, Charlottesville, VA, USA. [9]Flow Cytometry Core Facility, University of Virginia, Charlottesville, VA, USA.
*Corresponding author. Email: Makarand.Risbud@jefferson.edu
†These authors contributed equally to this work.

Histological analysis showed disc degeneration in SM/J at 6 M, which progressed in severity at 12 and 20 M, characterized by loss of nucleus pulposus (NP)/annulus fibrosus (AF) demarcation, decreased NP and AF cellularity, and increased AF clefts (Fig. 1, A to C‴). While differences in grading distribution were smaller at 6 M, there was a clear increase in higher, more degenerative grades by 20 M (Fig. 1, D and D′). As expected, both strains demonstrated age-associated lumbar disc degeneration; however, in SM/J, it was early onset and severe, evidenced by higher NP grades at 6 M and NP and AF grades at 12 and 20 M (Fig. 1, E and E′). Notably, ~90% of SM/J mice showed herniations at multiple lumbar levels by 20 M, with the highest incidence at L2-L5 (Fig. 1, F and G, and fig. S1A).

We investigated the impact of herniations on cell phenotype, survival, and local inflammation. Unlike BL/6, SM/J mice did not show quantifiable staining of the NP phenotypic marker CA3 (Fig. 1, H to H″) while showing an increased abundance of IL-6 in NP and AF (Fig. 1, I to I″). Furthermore, SM/J presented a higher percentage of terminal deoxynucleotidyl transferase–mediated deoxyuridine triphosphate nick end labeling (TUNEL)–positive cells, indicating compromised cell survival (Fig. 1, J to J″). These results show that SM/J mice experience accelerated age-dependent disc degeneration, with increased incidence of herniations accompanied by local inflammation, cell death, and loss of the NP cell phenotype.

Aged SM/J mice evidence alterations in matrix composition and remodeling

To understand extracellular matrix (ECM) health during aging and in the context of spontaneous herniations, collagen fiber thickness and markers of disc matrix integrity [collagen type II (COL2), cartilage oligomeric matrix protein (COMP), aggrecan proteoglycan (ACAN), and chondroitin sulfate (CS)] and degradation [ARGxx and matrix metallopeptidase 13 (MMP13)] were evaluated (*22*). Picrosirius red staining showed a lower proportion of thin fibers and a higher proportion of intermediate and thick fibers in 6-M SM/J discs (Fig. 1, K, K′, and N to N″, and fig. S1B). While no differences were observed at 12 M, at 20 M, a higher proportion of thin fibers, as well as a lower proportion of intermediate fibers, with significantly higher NP fibrosis was noted (Fig. 1, L′ to O, and fig. S1B). Notably, the collagen fiber thickness in SM/J discs remained relatively constant during aging; by contrast, in BL/6, a decrease in thin fibers and a concomitant increase in intermediate and thick fibers were noted, suggesting early-onset NP fibrosis in SM/J and age-associated AF collagen maturation in BL/6 (Fig. 1, N and O).

COL2 showed a marked reduction in abundance in NP and AF of 20-M SM/J mice (fig. S2, A to A″); however, COMP levels were comparable between the strains (fig. S2, B to B″). Notably, the abundance of ACAN, the primary disc proteoglycan, was lower in NP and AF compartments of SM/J mice (fig. S2, C to C″); however, the abundance of CS, a glycosaminoglycan side chain critical to the hydration of aggrecan and other sulfated proteoglycans, was decreased in the 20-M SM/J NP compartment but elevated in the AF at both 12 and 20 M, a characteristic feature associated with disc degeneration (fig. S2F). Moreover, a higher abundance of ARGxx, a maker of aggrecan degradation, and MMP13 was observed in SM/J discs (fig. S2, D to E″). These results indicate that SM/J herniations coincide with an altered ECM composition and increased catabolism.

AF tissue shows up-regulated DEGs associated with inflammatory activation before herniation onset but diminished immune activity in the context of persistent herniation

To investigate the molecular signatures associated with increased susceptibility to disc herniation, microarray analysis of the AF tissue before and after the onset of herniations was performed using 12-M SM/J (degenerated, nonherniated discs) and BL/6 (healthy discs) and after herniation using 20-M SM/J (degenerated, herniated discs) and BL/6 (degenerated, nonherniated discs) (Fig. 2, A and B). We focused our analysis on lumbar AF tissue on the basis of our previous studies of caudal disc phenotype in SM/J mice (high NP degeneration; no herniation) and tumor necrosis factor–α (TNF-α) transgenic mice (healthy NP phenotype; higher susceptibility to disc herniation), in which the NP degeneration status did not predict the susceptibility to disc herniation (*4*, *10*). Principal components analysis showed distinct strain- and aging-based profiles (Fig. 2B). The susceptibility of 12-M SM/J to developing hernia was associated with 2595 differentially expressed genes (DEGs) [46% up-regulated, 54% down-regulated, false discovery rate (FDR) < 0.05, and fold change (FC) ≥ 2.0] (fig. S3C), wherein up-regulated DEGs were enriched for B and T cell activation, inflammation, apoptosis, p53, Janus kinase/signal transducers and activators of transcription signaling, and angiogenesis; and down-regulated DEGs showed enrichment for the regulation of metabolic processes, innate response, response to stress, and ion transport (fig. S3, D to F), highlighting possible contributors to AF disruption and eventual disc herniation. While both SM/J and BL/6 up-regulated aging DEGs (FDR < 0.05 and FC ≥ 2.0) were enriched for T cell activation and apoptosis, SM/J aging down-regulated DEGs showed enrichment for the p53 pathway in contrast to BL/6 as well as cholecystokinin receptor and insulin/insulin-like growth factor (IGF) cascade (fig. S4A). To better understand the DEGs associated with the herniation phenotype independent of aging, we overlapped both up- and down-regulated DEGs of SM/J and BL/6 aging, uncovering unique genes in the SM/J group (herniation phenotype susceptibility) [602 (up) and 932 (down)], common aging genes between the strains [2894 (up) and 2832 (down)], and unique genes of the BL/6 group (fibrosis phenotype susceptibility) (Fig. 2, D and E, and table S1). Herniation susceptibility DEGs were enriched for distinctive clusters of biological pathways in comparison to disc aging and fibrosis comparisons (Fig. 2F and fig. S4, C and D). Up-regulated DEGs were associated with cell migration, positive regulation of phosphatidylinositol 3-kinase (PI3K) kinase, angiogenesis, collagen fibril organization, and shared axon guidance pathways with the fibrosis group. Down-regulated DEGs were associated with platelet-derived growth factor (PDGF) signaling, IGF cascade, PI3K, p53 pathway, and interleukin (IL)/inflammation mediated by chemokine and cytokine pathways, the last two of which were also associated with up-regulated DEGs in the fibrosis groups. These results supported the hypothesis that herniation pathophysiology differs from normal aging and fibrosis phenotypes.

Transcriptomic signatures of human AF degeneration share similarities with SM/J mice

To evaluate the clinical relevance of SM/J transcriptomic changes, we compared them with a previously reported dataset (GSE70362) of healthy, degenerated, and herniated human AF tissues (Fig. 2G) (*23*). The hierarchical clustering of these groups showed clear differences between healthy and degenerated/herniated tissues (fig. S5

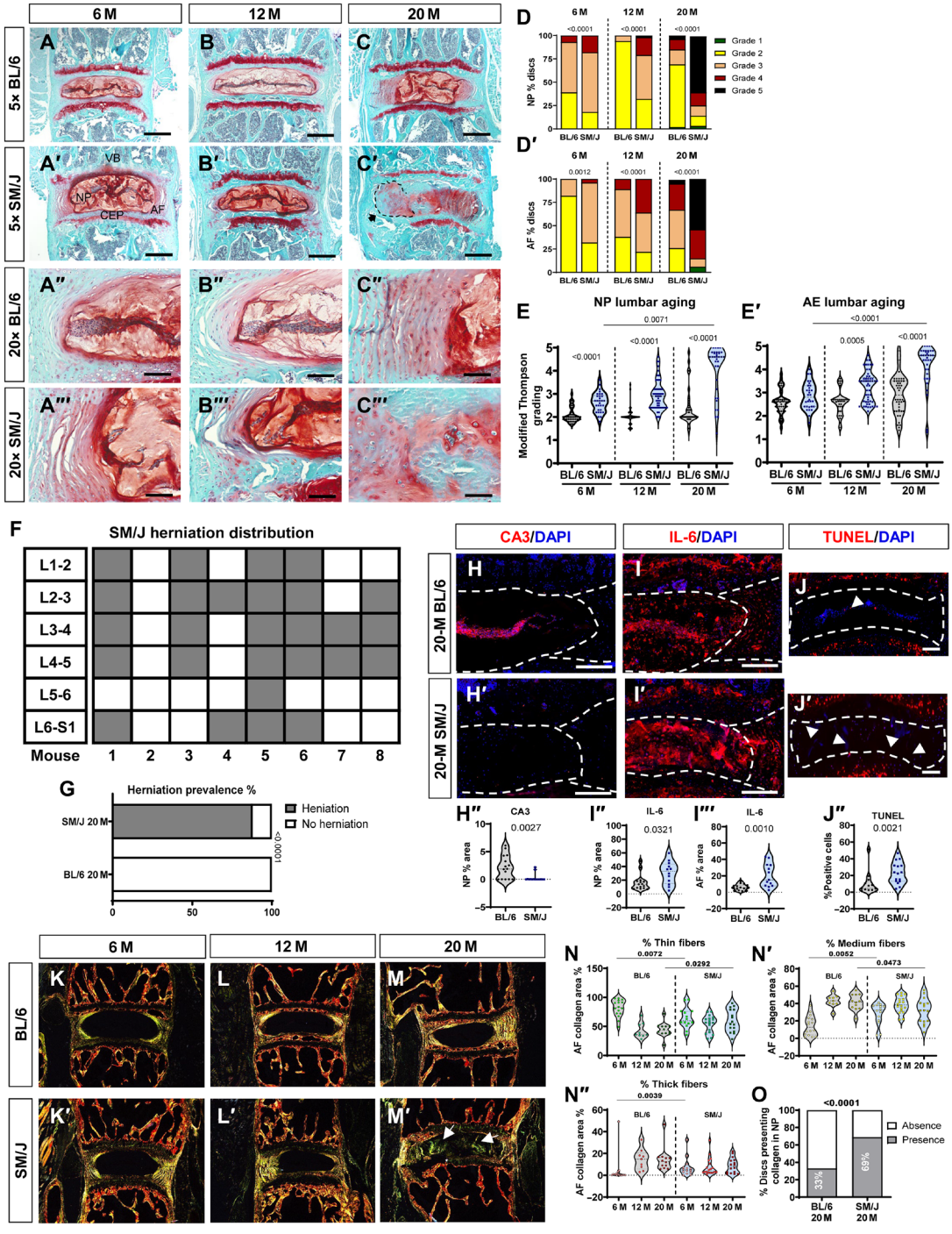

Fig. 1. SM/J mice show a high incidence of age-dependent disc herniation, accompanied by cellular deficiencies and matrix remodeling. (**A** to **C**″) Histology of the 6-, 12-, and 20-M-old BL/6 and SM/J lumbar discs. SM/J shows altered tissue architecture and cell morphology, indicating disc degeneration in the NP, AF, and cartilage end plate (CEP). (**D** to **E**′) Modified Thompson grade distributions and averages show higher average scores in SM/J NP and AF tissues. (**F** and **G**) Prevalence of herniations. Lumbar levels from L1-S1: $n_{BL/6\ 6\ M} = 5$ (3 females and 2 males); $n_{BL/6\ 12\ M} = 6$ (2 females and 4 males); $n_{BL/6\ 20\ M} = 9$ (3 females and 6 males); $n_{SM/J\ 6\ M} = 7$ (4 females and 3 males); $n_{SM/J\ 12\ M} = 10$ (6 females and 4 males); $n_{SM/J\ 20\ M} = 8$ (2 females and 6 males). (**H** to **J**″) Staining and abundance of key markers of (H to H″) NP cell phenotype (CA3), (I to I″) local inflammation (IL-6), and (J to J″) cell viability (TUNEL). BL/6: 12 M ($n = 5$ to 6 mice) and 20 M ($n = 5$ to 6 mice). SM/J: 12 M ($n = 5$ to 6 mice) and 20 M ($n = 5$ to 6 mice); two to three discs per animal. (**K** to **M**′) Picrosirius red staining and polarized light microscopy of lumbar disc sections. (**N** to **N**″) Analysis of percentage of thin (green), intermediate (yellow), and thick fibers (red). BL/6: 12 M ($n = 5$ to 6) and 20 M ($n = 5$ to 6). SM/J: 12 M ($n = 5$ to 6) and 20 M ($n = 5$ to 6); two to three discs per mouse. (**O**) Percentage of 20-M lumbar discs with collagen fibers in the NP. Kruskal-Wallis test for non-normally distributed data followed by Dunn's multiple comparison test was used for (E) and (E′), presenting adjusted *P* value. A two-tailed *t* test or Mann-Whitney test was used for (H″) to (J″) and (N) to (N″), and chi-square test was used for (D), (D′), (G), and (O). Scale bars (5×), 200 μm. Scale bars (20×), 200 μm.

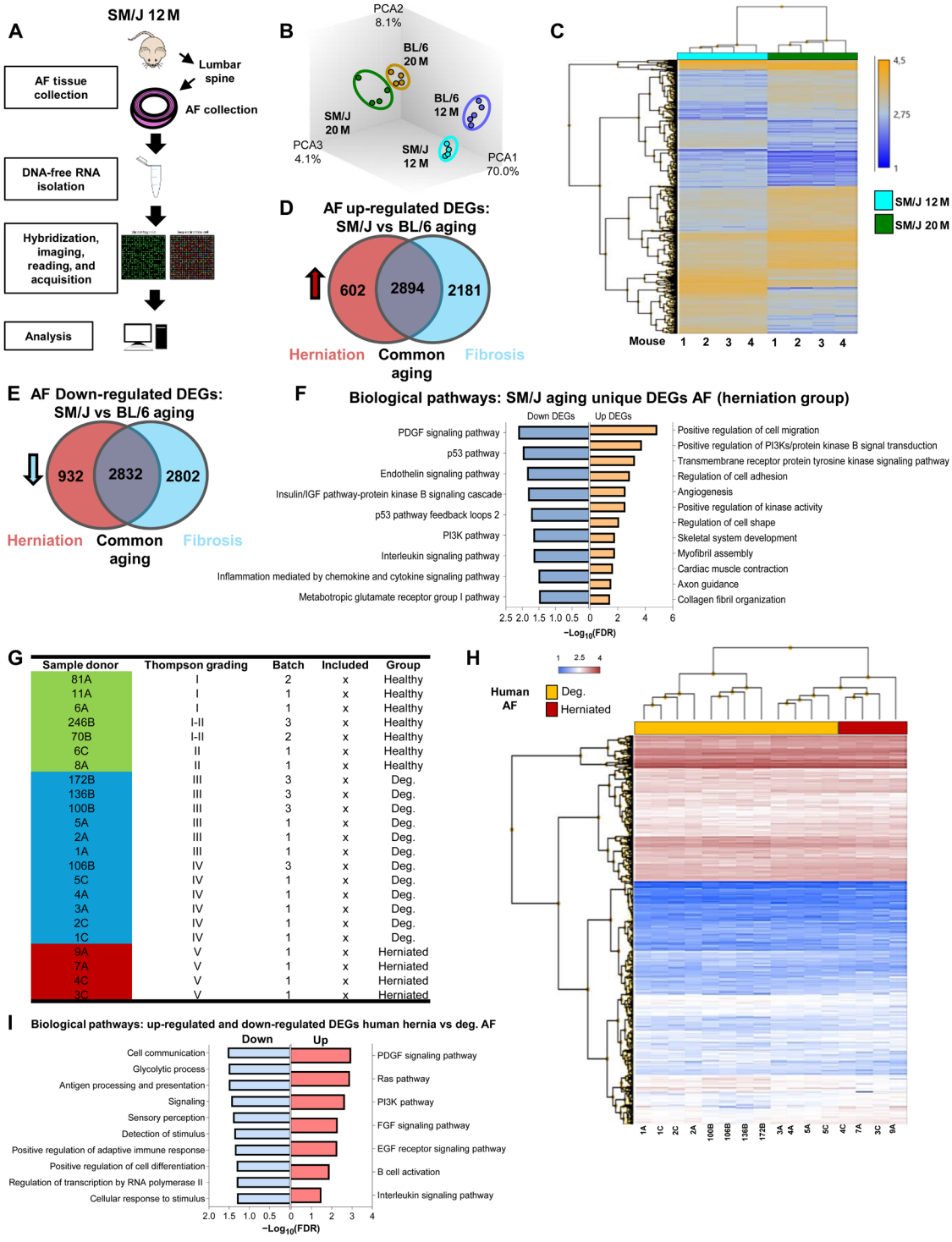

Fig. 2. Transcriptomic signatures of human AF degeneration share similarities with SM/J mice. (**A**) Schematic summarizing study design for the transcriptomic analysis of AF tissues. (**B**) Transcriptomic profiles of 12-M BL/6 AF ($n = 5$ mice), 20-M BL/6 AF ($n = 4$ mice), 12-M SM/J AF ($n = 4$ mice), and 20-M SM/J AF ($n = 4$ mice) tissues from mice clustered distinctly by principal components analysis. (**C**) Hierarchical clustering of SM/J aging DEGs (FC ≥ 2 and FDR ≤ 0.05). (**D**) Common and divergent up-regulated DEGs between SM/J AF and BL/6 AF aging. (**E**) Common and divergent down-regulated DEGs between SM/J AF and BL/6 AF aging. (**F**) Representative Panther Pathway processes from herniated group DEGs. (**G**) Human samples from GSE70362 included in the comparative analysis with SM/J. (**H**) Hierarchical clustering of herniated versus degenerated DEGs ($P \leq 0.05$). (**I**) Representative Panther Pathway processes from up- and down-regulated herniated versus degenerated DEGs. Panther analysis was performed using the PANTHER Overrepresentation Test with Panther Pathway and Panther Go Slim biological pathway database annotations and a binomial statistical test (FDR ≤ 0.05).

and S6). When degenerated and herniated samples were compared, a more complex relationship was revealed, with some degenerated samples more closely associating with herniated samples, reflecting that many herniated discs share features with discs exhibiting fibrotic degeneration (Fig. 2H). Up-regulated DEGs (hernia versus degeneration group) showed an enrichment for PDGF, Ras, PI3K, FGF (fibroblast growth factor), EGF (epidermal growth factor) receptor, B cell, and IL-associated pathways (Fig. 2I). By contrast, down-regulated DEGs were enriched for cell communication, glycolytic, antigen processing and presentation, sensory perception, and adaptive immune response (Fig. 2I). Of note, SM/J unique DEGs also presented modulation of PDGF, PI3K, and IL and similar association of immune response with down-regulated DEGs, suggesting species-independent biological pathways correlated with the herniation phenotype. To further investigate this, we determined common DEGs between human (degeneration, no hernia) versus 12-M SM/J (degeneration, no hernia) and human (degeneration, with herniation) versus 20 M SM/J (degeneration, with hernia). Common DEG lists are presented in figs. S5 to S7. Last, we used the CompBio tool to delineate commonality at the pathway level using the DEGs from the human herniated group and SM/J aging comparison (table S2) (*6*). These results suggest a degree of conservation between human and SM/J AF degeneration, highlighting shared molecular pathways underpinning this pathology.

SM/J mice show altered structural integrity of subchondral bony end plate

Sclerosis, increased bone mineral density, and decreased closed porosity of subchondral bone correlate with pain and local nerve growth in back pain and osteoarthritis models (*24*). Because of this proposed relationship between the disc and the structural integrity of adjacent vertebrae and subchondral bony end plate, morphological metrics of the L3-S1 vertebral subchondral bony end plate were analyzed. 20-M SM/J mice showed an accelerated osteoporotic phenotype, evidenced by decreased cortical and trabecular thickness and number (*4*). Subchondral bony end-plate volume did not differ between SM/J and BL/6 despite smaller vertebral size in SM/J (Fig. 3, A to C). This finding coincided with higher tissue mineral density and cortical thickness of end plates in SM/J males and a higher bone volume fraction in females and males (Fig. 3, D to F). In addition, SM/J males showed lower bone surface complexity and closed porosity (Fig. 3, G and H).

SM/J mice show peripheral vascularization and innervation of the herniated discs

Disc herniation is tightly correlated with cLBP and radiculopathy. Neurofilament, a marker of axonal ingrowth (*16*), and endomucin, a marker of neovascularization commonly associated with neoinnervation (*15*), were used to investigate nerve and blood vessel ingrowth in herniated SM/J discs. We observed that endomucin- and NF-stained structures were in proximity outside the disc at 12 M but were present within the outer AF of herniated discs in 20-M SM/J (Fig. 3, I to J″). Endomucin staining was pronounced in more 20-M-old SM/J mice compared to age-matched BL/6 controls, suggesting increased vascularization in this group (Fig. 3J). These results confirm an association between disc herniation and local axonal and blood vessel ingrowth, as reported in humans (*25*). In addition, neuronal and pain marker NGF was significantly higher in 20-M SM/J NP and AF tissues than in 20-M BL/6 (Fig. 3, K to L″), suggesting that herniations in SM/J mice may stimulate neuropathic pain.

SM/J mice show increased sensitization to mechanical and cold stimuli, along with changes in gait

Human herniation is often associated with several neuropathic symptoms, including paresthesia, allodynia, hyperalgesia, and heat sensitization (*26*, *27*). To assess similar behavioral changes, mechanical (Von Frey filament) and temperature (Hargreaves thermal; cold plantar assay) sensitization was measured in SM/J and BL/6 mice (*28*, *29*). Compared to BL/6, SM/J mice demonstrated a lower threshold for mechanical stimulation inducing a pain-like response during aging (Fig. 3M). In addition, SM/J showed a decreased latency for a noxious cold stimulus inducing a pain-like response than BL/6 at 12 and 20 M (Fig. 3N). By contrast, Hargreaves testing (heat sensitivity) showed increased desensitization in 12-M SM/J mice, which persisted at 20 M (Fig. 3O). To study the correlation of gait features with neurological pathologies or locomotion-related pain, gait analysis was performed (Fig. 3P) (*30*). SM/J mice presented an age-dependent increase in swing time; however, compared to BL/6, the swing time was shorter in SM/J, independent of age (Fig. 3Q). Paw angle variability increased with age in BL/6, and a similar trend was observed in SM/J mice (Fig. 3R). While the stance width variability rose with age in BL/6, it remained lower than in SM/J at 12 M (Fig. 3S). There were no significant changes in other parameters associated with ataxia (step angle and stride length variability), impaired mobility (swing duration), limb injury (paw area peak stance), or gait symmetry (Fig. 3, T to X). These findings show that SM/J replicates clinical behaviors commonly seen in human patients with disc herniation and radiculopathy.

SM/J DRGs show enrichment of DEGs associated with the glial cells, neuroinflammatory response, cell-matrix adhesion modulation, and immune system regulation

To study the molecular changes in DRGs concordant with herniation and behavioral changes, transcriptomic analysis of lumbar DRGs was performed. While SM/J profiles diverged with age, BL/6 profiles did not mirror this separation (Fig. 4A). Source-of-variation analysis showed that the compounded effects of age and strain ("Condition") were the highest source of variation among samples, whereas sex-based effects were negligible in both strains (Fig. 4B). Hierarchical clustering of 12-M SM/J and BL/6 showed divergent transcriptomes between the strains (fig. S8A). There were 188 up-regulated DEGs (FDR < 0.05 and FC ≥ 2), which did not enrich in any biological pathways (PantherDB) (fig. S8, B and C), whereas 167 down-regulated DEGs were associated with the response to interferon-β (IFN-β), positive regulation of response to a biotic stimulus, activation of the innate immune response, antigen processing, and presentation of peptide antigen pathways (fig. S8, B and C). Comparison of DEGs from 20-M SM/J with 12-M SM/J showed distinct clustering during aging (fig. S9A), and a total of 401 DEGs was noted (327 up-regulated and 74 down-regulated) (fig. S9B). There was no biological enrichment within the down-regulated DEGs; however, up-regulated DEGs were associated with ECM organization and adhesion regulation; modulation of IL-1, IL-4, IL-6, IL-10, and IL-12; regulation of IFN-α and transforming growth factor–β pathways; synapse pruning; cellular response to amyloid-β; regulation of neuron death; astrocyte activation and microglial cell migration; Toll-like receptor; and negative regulation of B cell receptor signaling (fig. S9, B and C).

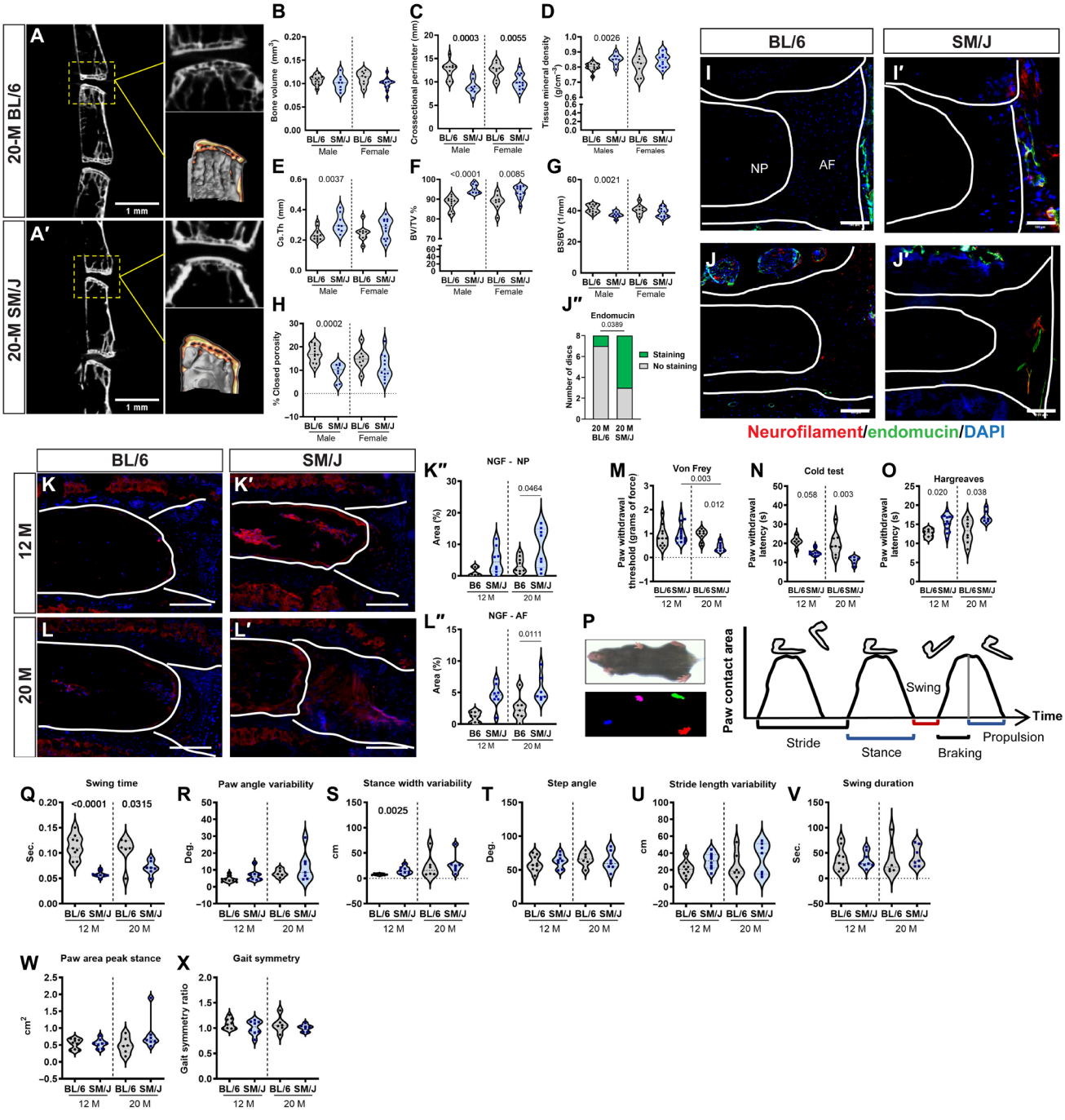

Fig. 3. SM/J mice show an altered subchondral bone structure, tissue innervation, and altered sensitivity to mechanical and temperature stimuli with aging. (**A** and **A**′) Microcomputed tomography reconstruction of 20-M BL/6 and SM/J vertebrae, with the marked subchondral bone region of interest. (**B** to **H**) Analysis of subchondral bony end-plate parameters: (B) bone volume, (C) cross-sectional perimeter, (D) tissue mineral density, (E) cross-sectional thickness, (F) bone volume (BV/TV), (G) bone surface/volume (BS/BV), and (H) % closed porosity between 20-M BL/6 and SM/J males and females. $n_{BL/6\ female} = 2$; $n_{BL/6\ male} = 3$; $n_{SM/J\ female} = 2$; $n_{SM/J\ male} = 2$; four vertebrae (L3-L6 per mouse). Two-tailed *t* test or Mann-Whitney test was used as appropriate. (**I** to **J**″) Neurofilament and endomucin presence in BL/6 and SM/J discs at 12 and 20 M, with the endomucin presence quantified. $n = 6$ to 8 mice per strain; two to three levels per mouse. Scale bars, 200 μm. (**K** to **L**″) Quantified NGF staining (K to L′) in 12- and 20-M BL/6 and SM/J NP (K″) and AF (L″) tissues. (**M** to **O**) Sensitization analysis: (M) mechanical (Von Frey), (N) hot (Hargreaves), and (O) cold stimulus. $n_{BL/6\ 12\ M} = 6$ to 11; $n_{BL/6\ 20\ M} = 8$; $n_{SM/J\ 12\ M} = 11$ to 14; $n_{SM/J\ 20\ M} = 6$ to 7. (**P**) Schematic of gait analysis and parameters. (**Q** to **X**) Gait parameters: (Q) swing time, (R) paw angle variability, (S) stance width variability, (T) step angle, (U) stride length variability, (V) swing duration, (W) paw area peak stance, and (X) gait symmetry. $n_{BL/6\ 12\ M} = 9$; $n_{BL/6\ 20\ M} = 6$; $n_{SM/J\ 12\ M} = 8$; $n_{SM/J\ 20\ M} = 7$. Kruskal-Wallis test for non-normally distributed data followed by Dunn's multiple comparison test was used for (M) to (O), with adjusted *P* value. Two-tailed *t* test or Mann-Whitney test was used to compare differences between two groups as appropriate for (B) to (H), (K′) to (L″), and (K) to (X). Chi-square test was used for (J″). (I to J′) Scale bars (20×), 200 μm. (K to L′) Scale bars (10×), 200 μm.

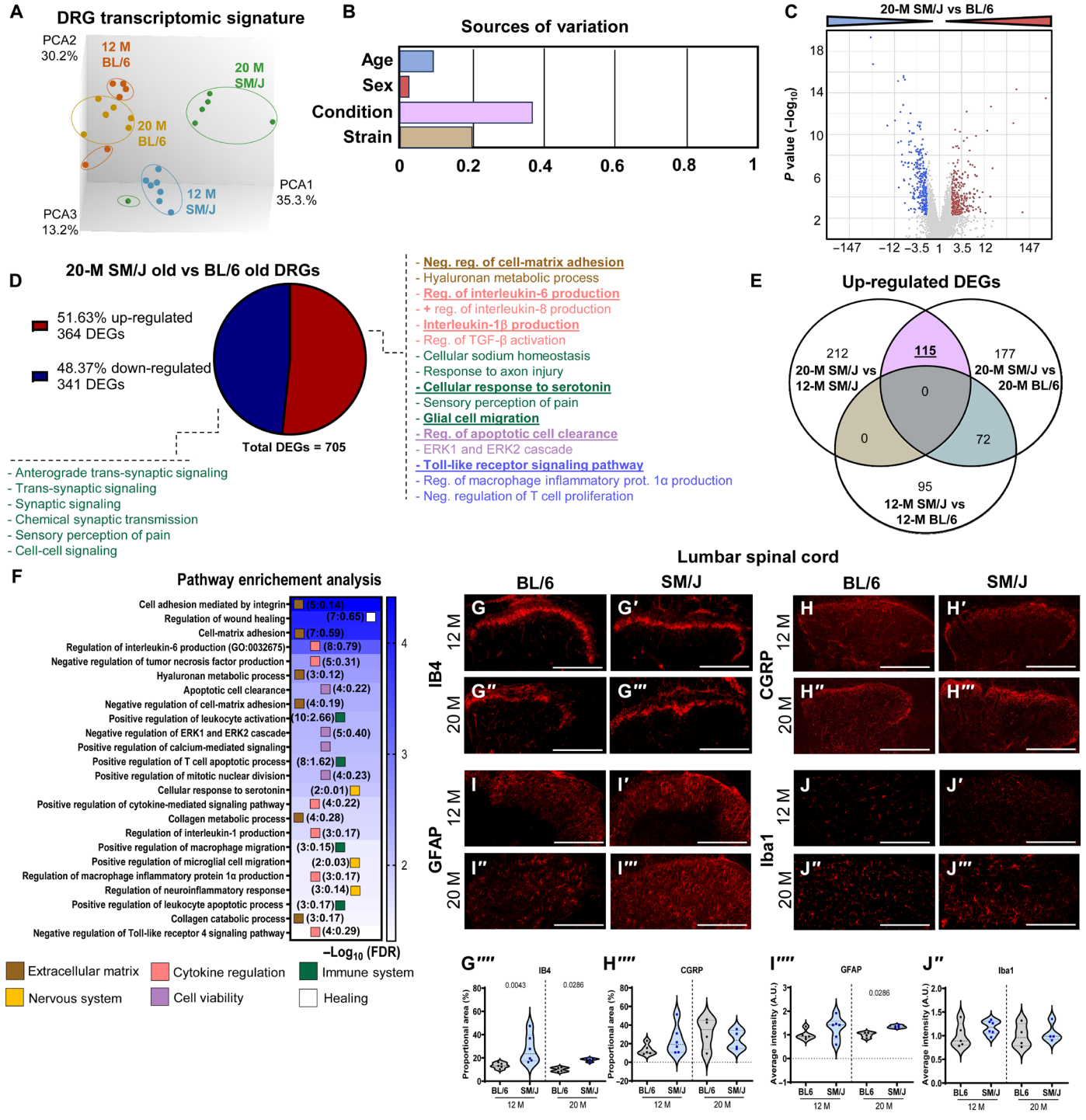

Fig. 4. DRGs in SM/J mice show the enrichment of DEGs associated with the glial cells, neuroinflammatory response, cell-matrix adhesion modulation, and immune system regulation. (**A**) Principal components analysis of transcriptomic profiles of 12- and 20-M BL/6 ($n = 3$ females and 3 males per time point) and SM/J ($n = 3$ females and 3 males per time point) DRG tissues, (**B**) weighted source of variation, and (**C**) volcano plot showing up- and down-regulated DEGs from the 20-M SM/J DRGs versus 20-M BL/6 DRG comparison (FC ≥ 2 and FDR ≤ 0.05). (**D**) Pie chart showing the distribution of up- and down-regulated DEGs and enriched GO processes from the 20-M SM/J versus BL/6 DRGs. (**E**) Venn diagram of common up-regulated DEGs in 20-M SM/J versus 12-M SM/J and 20-M SM/J versus 20-M BL/6 but not present in 12-M SM/J versus 12-M BL/6. (**F**) Pathway enrichment analysis of 115 DEGs identified in (E); analysis performed in PantherDB using the statistical overrepresentation test with Gene Ontology database annotations and a binomial statistical test (FDR < 0.05). Values in parentheses demonstrate the number of genes within the annotation set relative to the predicted number of genes. (**G** to **J‴**) Quantitative immunohistochemistry of the dorsal horn of the spinal cord in the lumbar region: (G to G‴) IB4, (H to H‴) CGRP, (I to I‴) GFAP, and (J to J‴) IBA1. A.U., arbitrary units. $n_{BL/6\ 12\ M} = 6$; $n_{BL/6\ 20\ M} = 4$; $n_{SM/J\ 12\ M} = 6$; $n_{SM/J\ 20\ M} = 4$; two spine levels per animal. Two-tailed *t* test or Mann-Whitney test was used as appropriate. Nonparametric Spearman correlation test was used for analysis in (D) to (G). Scale bars (A to H′), 200 μm.

Hierarchical clustering of 20-M SM/J versus BL/6 showed clear strain-based segregation of DEGs (fig. S9A) with 364 up-regulated and 431 down-regulated DEGs in SM/J (Fig. 4D). Up-regulated DEGs (fig. S10B) showed enrichment of negative regulation of cell-matrix adhesion and hyaluronan metabolic process; regulation of IL-1β, IL-6, and IL-8; transforming growth factor–β activation; response to axon injury; cellular response to serotonin; glial cell migration; sensory perception of pain signaling; regulation of apoptotic cell clearance; ERK1 (extracellular signal–regulated kinase 1) and ERK2 cascade; modulation of Toll-like receptor signaling; macrophage inflammatory protein 1α production; and negative regulation of T cell proliferation (Fig. 4D). Down-regulated DEGs (fig. S10B) were enriched for trans-synaptic signaling, sensory perception of pain, and other signaling pathways (Fig. 4D).

To identify any DEGs associated with the pain-related behaviors exhibited by 20-M SM/J and to minimize the effect of age- and strain-based variation, we investigated the DEGs common between the SM/J aging and 20-M SM/J versus BL/6 comparisons and subtracted the baseline strain-associated DEGs identified from 12-M SM/J versus BL/6 comparison (Fig. 4E and fig. S1L). Eight down-regulated transcripts, *Gp1bb*, *Spry3*, *Izumo4*, *Ephx4*, *Plpp4*, *Foxj1*, *Prrt2*, and *Arhgdig* (fig. S11, A and B), and 115 up-regulated DEGs met these criteria (Fig. 4E). Consistent with the observed pathophysiology of SM/J mice in this study, these DEGs were associated with the ECM, cytokines, nervous system, cell viability, and immune regulation pathways (Fig. 4F). These results provide new insight into the pathological processes in DRGs in this novel model of spontaneous disc herniation.

SM/J mice show higher staining for IB4 and GFAP in the lumbar dorsal horn

We evaluated the abundance of IB4-binding (nonpeptidergic) and CGRP-positive (peptidergic) nociceptive axons in the dorsal horn of the thoracic (adjacent to nonherniated discs) and lumbar (herniated) spinal cord (*16*). In the lumbar region, an abundance of IB4-positive axons was higher in SM/J mice at 12 and 20 M, whereas the abundance of CGRP-positive axons was maintained across all groups (Fig. 4, G to H″″). Microglia and astrocytes play essential roles in pain modulation, and the reactivity of these cell types in the spinal cord dorsal horn is associated with multiple chronic pain states (*17*, *31*). No differences were observed in levels of the microglial marker Iba1, but 20-M SM/J showed higher levels of the reactive astrocytic marker glial fibrillary acidic protein (GFAP) (Fig. 4, I to J″). This increase in GFAP abundance coincided with a broader spatial distribution of astrocytes in the deeper layers of the dorsal horn, something not observed in BL/6 or 12-M SM/J mice. By contrast, no significant changes were observed in these markers in the thoracic region (fig. S11, D and E). These findings suggest a possible role of IB4 nociceptive neurons and astrocytes in pain sensitization in SM/J mice with herniations.

SM/J mice show altered plasma cytokine levels and increased T cell and neutrophil recruitment in the vertebral marrow

We assessed the impact of strain and aging on the systemic burden of inflammation by evaluating the abundance of pro- and anti-inflammatory markers. Plasma levels of IL-10, IL-15, IL-17A, IL-18A/F, IL-1β, IL-27p28/IL-30, monocyte chemoattractant protein 1, and macrophage inflammatory protein–3α (MIP-3α) rose during aging in BL/6 (Fig. 5, A to R, and fig. S11). While SM/J showed a similar increase in IL-17A and MIP-3α levels with aging, an increase in IL-16, IL-33, and MIP-1α was also noted (Fig. 5, P and Q, and fig. S12). 12-M SM/J had higher baseline levels of IL-21, IL-23, and IL-6 than BL/6 (Fig. 5, H, I, and L, and fig. S12). At 20 M, SM/J evidenced lower IL-2, IL-4, and IFN-γ compared to BL/6. Levels of IL-17C, IL-22, IL-5, IL-9, IP-10 (IFN-γ–induced protein 10), keratinocyte chemoattractant/human growth-regulated oncogene (KC/GRO), and MIP2 were consistent among all groups. Notably, IFN-γ, IL-1β, IL-2, and IL-4 showed a negative correlation to sensitization to mechanical stimuli (Fig. 5, S to V). We evaluated the recruitment of B cells (CD19), T cells (CD3), neutrophils (Ly6G), macrophages (F4/80), and activated T cells and macrophages [major histocompatibility complex class II (MHCII)] in the vertebral marrow (*32*). While no changes were observed in CD19, F4/80, or F4/80-MHCII double-positive cells, CD3 and MHCII abundance was higher in 20-M SM/J mice than in age-matched BL/6 and 12-M SM/J mice (Fig. 5, W to Z). Higher levels of Ly6G in 20-M SM/J mice relative to 20 M BL/6 mice were also observed (Fig. 5, W to Z). These studies support the idea that the immune system contributes to disc herniation–associated radiculopathy.

SM/J mice show altered immune cell profiles in peripheral circulation

Immune cells are key modulators of cLBP development (*13*). To investigate the circulating immune cell profile and understand their association with pain pathology in SM/J mice, we performed a single-cell RNA sequencing (scRNA-seq) of peripheral blood mononuclear cells (PBMCs) (Fig. 6A). After normalization, the cells were grouped into 21 clusters according to the FindNeighbors and FindClusters functions within the Seurat single-cell sequencing analysis package (Fig. 6A). Furthermore, the data were visualized according to age and strain and cell types were labeled using the SingleR annotation tool, demonstrating (*33*) marked changes in cell populations across strains and with aging (Fig. 6, B to C″, and fig. S9A). No major changes in the distributions of cell types were observed across strains at 12 M, but by 20 M, SM/J showed lower proportions of monocytes and T cells and higher proportions of B cells and macrophages than BL/6 (Fig. 6, C to C″).

Previous studies have suggested the dependence of immune cell heterogeneity on inflammatory versus quiescence state, function, and origin (*34*, *35*). To visualize heterogeneity, cell populations were subset and visualized with uniform manifold approximation and projection (UMAP), showing distinct differences in cell populations according to pain status–specific differences—B cells and macrophages (Fig. 6, D and E, and fig. S13, B and C)—and strain—T cells (subdivided into CD4+ and CD8a+ T cells), monocytes, natural killer (NK) cells, and granulocytes (fig. S14). Gene set enrichment analysis (GSEA) was conducted on DEGs defined by $P < 0.05$ for each cell population using the clusterProfiler package (*36*). In B cells of 20-M SM/J, GSEA showed the activation pathways related to T cell tolerance induction, Ras protein signal transduction, and immune system processes (Fig. 6F′ and fig. S13, B′ and B″). On the other hand, B cells showed suppression of negative regulation of regulatory T cell differentiation and purine biosynthesis process, and top DEGs included *Bach2*, *Cmss1*, *Ripor2*, *Ebf1*, and *Cdk8* (Fig. 6, D′ and D″, and fig. S14, B′ and B″). While the proportion of macrophages in the pain group was higher, their DEGs showed suppression of defense- and immune response–related pathways and activation of platelets, blood coagulation, and serotonin uptake, with top DEGs including

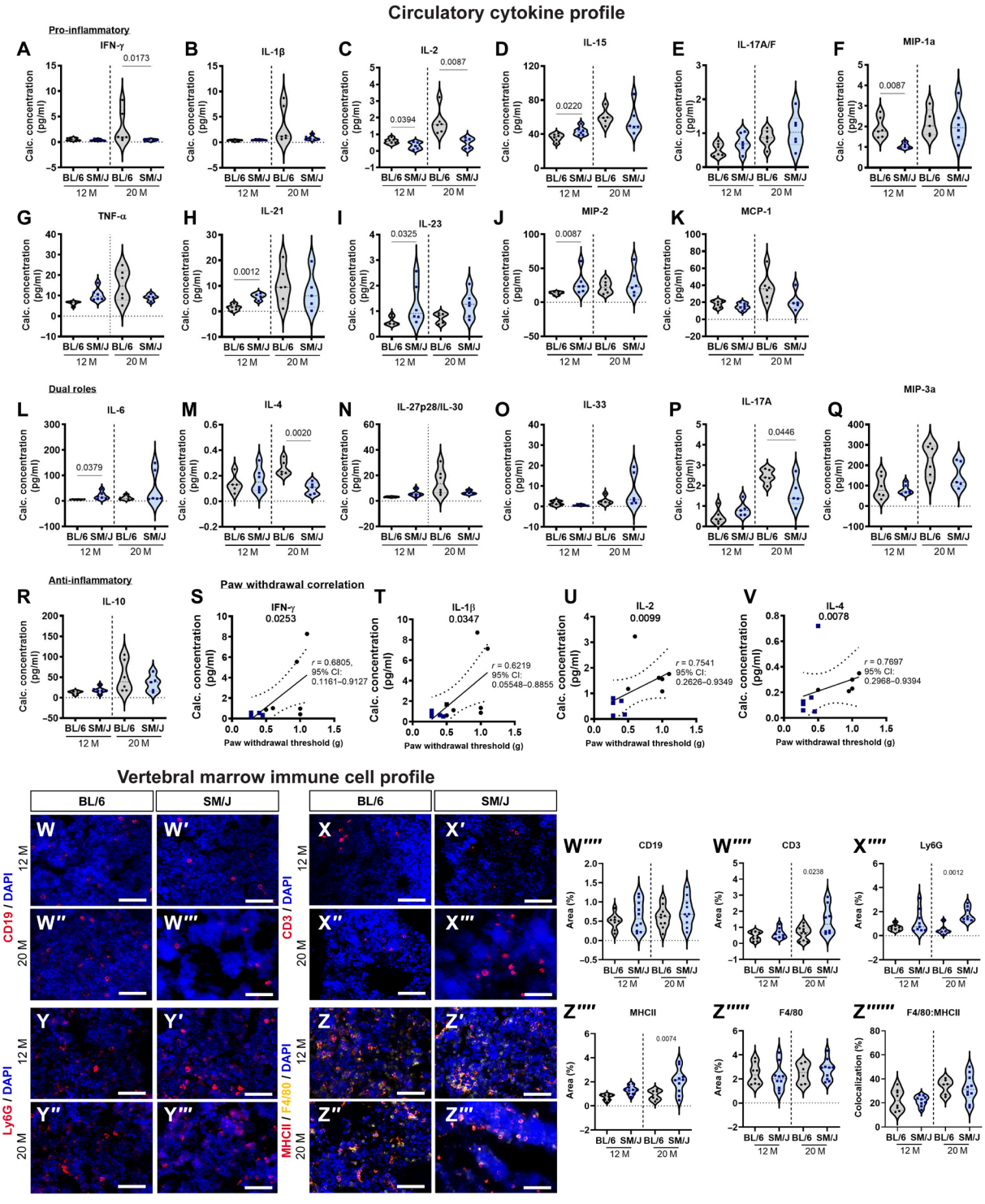

Fig. 5. SM/J mice show altered plasma cytokine levels and increased T cell and neutrophil recruitment in the vertebral marrow. (**A** to **R**) Multiplex analysis of pro-inflammatory, dual function, and anti-inflammatory proteins in plasma from 12- and 20-M BL/6 and SM/J mice. *t* test or Mann-Whitney test was used as appropriate. (**S** to **V**) Pearson correlation between INF-γ, IL-1, IL-2, and IL-4 plasma levels and Von Frey sensitivities. $n = 4$ to 6 mice per strain per time point. (**W** to **Z**‴″) Quantitative immunohistochemistry of (W to W‴″) CD19, (X to X‴″) CD3, (Y to Y‴″) Ly6G, and (Z to Z‴″) MHCII and F4/80 (individually and ratio quantification) at 12 and 20 M in the vertebral bone ($n = 6$ to 10 vertebrae per strain per time point). Two-tailed *t* test or Mann-Whitney test was used as appropriate. Scale bars (A to H′), 100 μm.

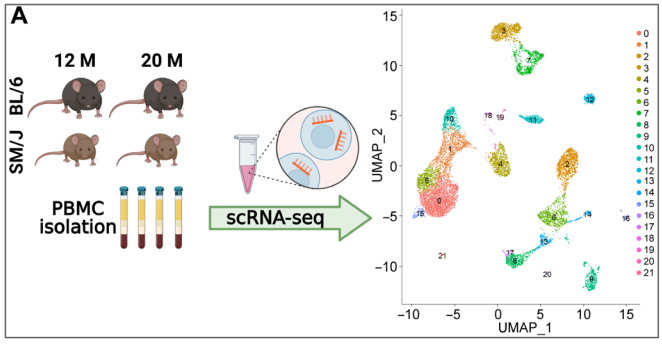

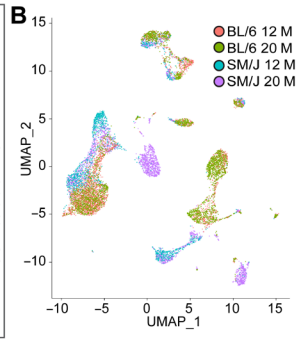

C

	BL/6 12 M	BL/6 20 M	SM/J 12 M	SM/J 20 M
B cells	59.36%	32.84%	56.47%	61.33%
Dendritic cells	0.09%	0.23%	0.12%	0.08%
Endothelial cells	0.12%	0.16%	0.04%	0.04%
Erythrocytes	0.09%	0.06%	0.58%	0.19%
Fibroblasts	0.00%	0.00%	0.00%	0.08%
Granulocytes	2.98%	4.31%	1.12%	0.93%
Macrophages	2.74%	3.47%	2.70%	14.99%
Monocytes	18.32%	38.85	21.16%	11.12%
NK cells	4.40%	3.09%	2.82%	2.21%
T cells	11.90%	16.98%	14.98%	9.03%

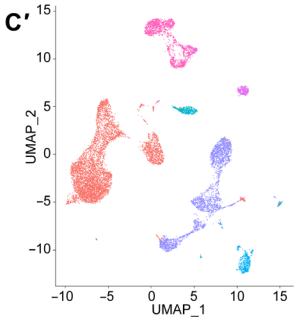

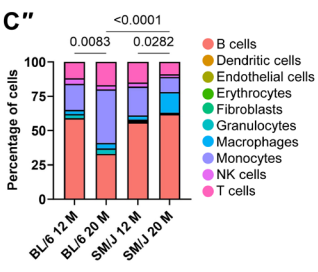

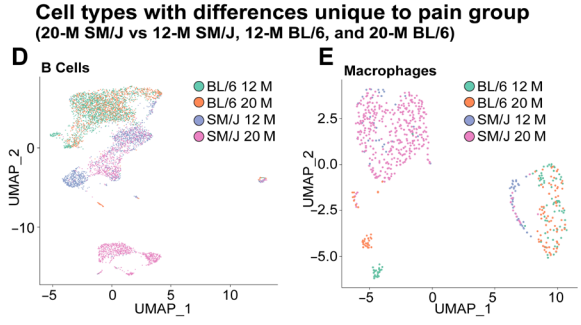

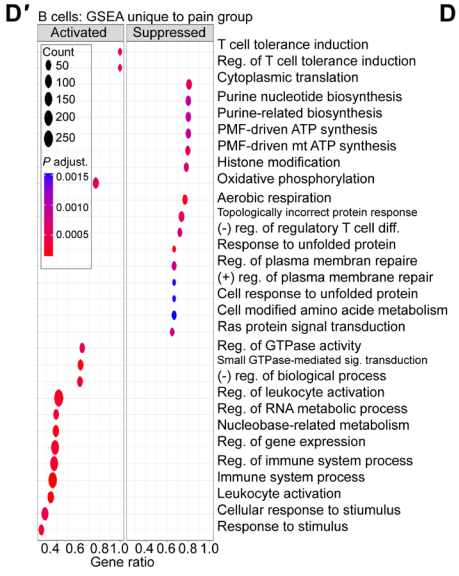

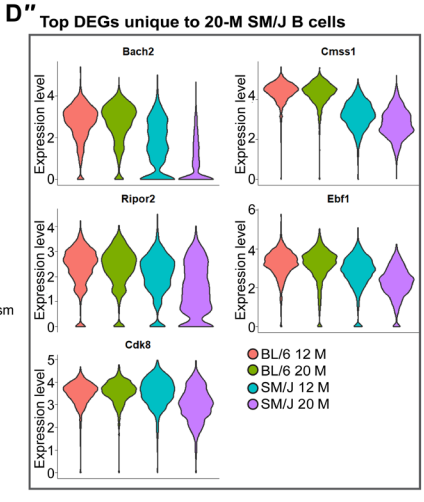

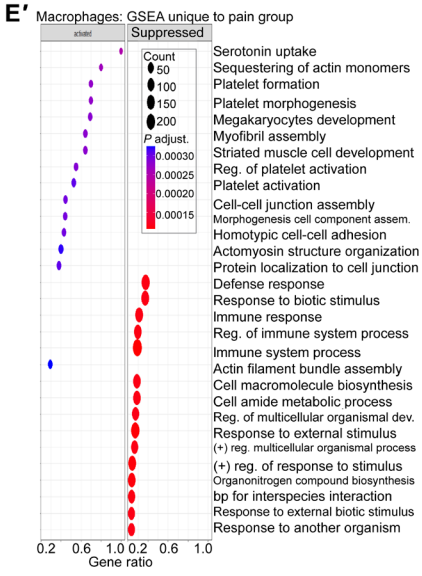

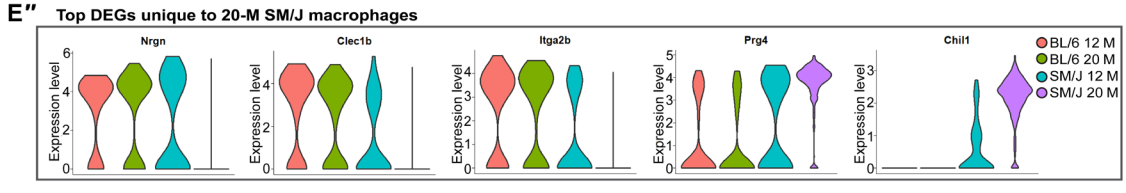

Fig. 6. SM/J mice show altered immune cell profiles in peripheral circulation. (**A**) Schematic showing experimental design and unbiased clustering of PBMC transcripts. $n_{12\,M\,BL/6} = 2$ females and 2 males; $n_{12\,M\,SM/J} = 2$ females and 1 male; $n_{20\,M\,BL/6} = 2$ females and 2 males; $n_{20MSM/J} = 4$ males. (**B**) Clustering of PBMC transcripts according to strain and time point. (**C** to **C**″) Proportion of cell populations labeled with the SingleR program. (**D** and **E**) UMAP labeled according to mouse strain and age, showing cell populations identified to be unique to SM/J at 20 M, when mice show disc herniations and pain behaviors: (D) B cells and (E) macrophages. (**D**′) GSEA in B cells based on DEGs identified in 20-M SM/J PBMCs. (**D**″) Violin plots of most DEGs in B cells in the SM/J pain group. (**E**′) GSEA of macrophages from 20-M SM/J. (**E**″) Violin plots of most DEGs in macrophages in the SM/J pain group (n ~ 5000 cells per strain per time point). Chi-square test was used for (C″).

Nrgn, *Clec1b*, *Itga2b*, *Prg4*, and *Chil1* (Fig. 6, E′ and E″, and fig. S14, E′ and E″). SM/J CD4+ T cells showed DEGs associated with intracellular molecular regulation–related pathways (fig. S14B′). Despite being fewer in the 20-M SM/J group, CD8+ T cells were enriched for the activation of an innate response, positive regulation of leukocyte-mediated cytotoxicity and immunity, and cellular response to IFN-γ and for suppression of negative regulation of Wnt signaling, translation, and complement activation (fig. S14C′). GSEA of SM/J monocytes showed activation of positive regulation of T cell activation, antigen processing and presentation, and lymphocyte-mediated immunity and suppression of response to a stimulus and regulation of biological processes (fig. S13E′). Last, SM/J NK cells were enriched for the activation of the innate immune response, NK cell–mediated immunity, and apoptotic cell clearance (fig. S14F′).

To explore the agreement between scRNA-seq and plasma analyses, we looked for cell populations expressing *Ifng*. We found T cells and NK cells to be the two predominantly *Ifng*-expressing populations, and trends in expression, considered with the cell population trends, confirm the reduced overall expression in 20-M SM/J mice (fig. S15, A to A″). These analyses suggest that dysregulation of the immune system, characterized by suppression of basic immune and regulatory processes in multiple cell types, of SM/J mice contributes to chronic disc herniation and pain.

SM/J mice show an altered immune cell profile in the spleen

To further interrogate the associations between discogenic and radicular pain and the systemic immune system modulation, cytometry by time-of-flight (CyTOF) analysis was conducted on splenocytes from 12- and 20-M mice using 16 cell-surface markers and 8 intracellular cytokines (20 M only); a previous study has shown that the splenocyte profile reliably correlates with the systemic adaptive immune response (*37*). Using established immune cell signature profiles, 15 cell populations were identified on the basis of an initial gating for CD45+ cells (Fig. 7A). This cell identification strategy also coincided with our scRNA-seq data, aligning with several populations identified in that analysis (fig. S16B). At 12 M, SM/J showed a significantly higher frequency of T cells and NK cells than BL/6 (Fig. 7B and fig. S16, A to A‴), whereas at 20 M, this trend reversed for NK cells and there was no difference between two strains for overall T cell numbers. However, among T cells, there was a higher frequency of the CD8+ T cells in SM/J splenocytes (Fig. 7, B′ to C′, and figs. S16, B to B‴, and S11). During aging, the NK cell frequency rose, and CD8+ T cell and myeloid cell frequencies decreased in BL/6 (Fig. 7C and fig. S16, C to C‴). Frequencies of NK cells, CD4+ memory T cells, and CD4+ naïve T cells decreased during aging in SM/J (Fig. 7, C′ to I, and fig. S16, D to D‴).

To investigate possible functional differences in the immune cell populations in mice with herniated discs, intracellular cytokine levels were determined at 20 M (Fig. 7J and fig. S17). At 20 M, SM/J mice showed significantly higher numbers of myeloid cells producing IFN-γ (Fig. 7K). These inflammatory myeloid cells that include granulocytes, monocytes, and macrophages (M1 macrophages) depicted that an inflammatory type 1 immune response [T helper 1 (T_H1) response] characterized by IFN-γ production was predominant in SM/J mice. Lower production of anti-inflammatory T_H2 cytokines IL-4 and IL-5 in plasmacytoid dendritic cells (Fig. 7L) and CD8+ naïve T cells (Fig. 7M), respectively, corroborated the inflammatory environment. IL-2 was also lower in conventional dendritic cells (Fig. 7N). Furthermore, nonspecific activation of CD8+ T cells (Fig. 7O) and CD8+ memory T cells (Fig. 7P) was also observed. Overall, there was enhancement of an inflammatory T_H1 response and suppression of an anti-inflammatory T_H2 immune response. The T_H17 immune response was also suppressed, as seen by significantly lower production of IL-17A by Lin− cells (Fig. 7Q) as well as myeloid cells (Fig. 8A), indicating that an inflammatory T_H1 immune response, not T_H17, underscored the phenotype. Significant changes in cytokine profiles of other cell populations were not observed (fig. S12).

DISCUSSION

Intervertebral disc degeneration comprises multiple degenerative phenotypes (*3*). Recently, SM/J mice were shown to evidence early-onset, spontaneous disc degeneration characterized by advanced fibrosis in the caudal spine during aging compared to BL/6 and LG/J strains that show milder fibrosis and dystrophic calcification, respectively (*4*, *19*). These studies highlight the essential contribution of genetic background to degenerative processes, reinforcing findings from human twin studies that show that familial background is a larger contributor to disc degeneration than aging and mechanical loading (*21*). This study shows that SM/J mice are highly susceptible to age-associated lumbar disc herniations. These results suggest that while genetics govern susceptibility to disc degeneration, anatomical/mechanical factors may influence and drive the final degenerative outcome (*4*). This idea aligns with studies of LG/J mice that show age-dependent calcification restricted to the caudal spine (*4*) and a significantly higher prevalence of disc degeneration at L3-5 of the human spine than the other levels (*3*). However, the effect of genetic background and age as independent variables in this study must not be overlooked. The SM/J susceptibility to disc herniation aligns with previous genome-wide association studies in this model and the Twin Spine Study, suggesting genetic background as the primary modulator of regeneration potential and disc degeneration process (*21*, *38*). In humans, it is acknowledged that spinal lordosis and unit rigidity make L3-4 and L4-5 levels more susceptible to herniation, but with aging and a consequent decrease in lordotic angle, the prevalence increases in the upper lumbar levels (*39*, *40*). In line with these clinical findings, our study describes a model of spontaneous disc herniation associated with aging, which may explain a higher herniation frequency in upper lumber levels. While we cannot state with certainty the precise contribution of mechanics or lordosis in SM/J mice, it is important to highlight that the mechanics, tissue structure, and even embryonic signaling change across the mouse spine, which precede the regional susceptibilities across the spine (*41*–*43*). It is also true that multilevel disc herniation is less prevalent in humans, with sources reporting 53 to 80% of herniations as a single level, 12 to 22% as two levels, and fewer presenting more than three affected levels (*44*, *45*). However, these generalizations may include a selection bias, as studies evaluating the thoracic region and older patients show increased incidence of multilevel disc herniation (*46*, *47*). Unfortunately, there are very little data on the prevalence and distribution of intervertebral disc herniation in the elderly population. In this sense and understanding of the impossibility of an animal model fully capturing every feature of human disease, SM/J mice present a unique opportunity for study, recapitulating the increased susceptibility to disc herniation with aging. Of note, 20-M-old mice correspond to elderly humans aged about 60 to 65 years old. In addition, previous work by Rajasekaran *et al.* (*48*)

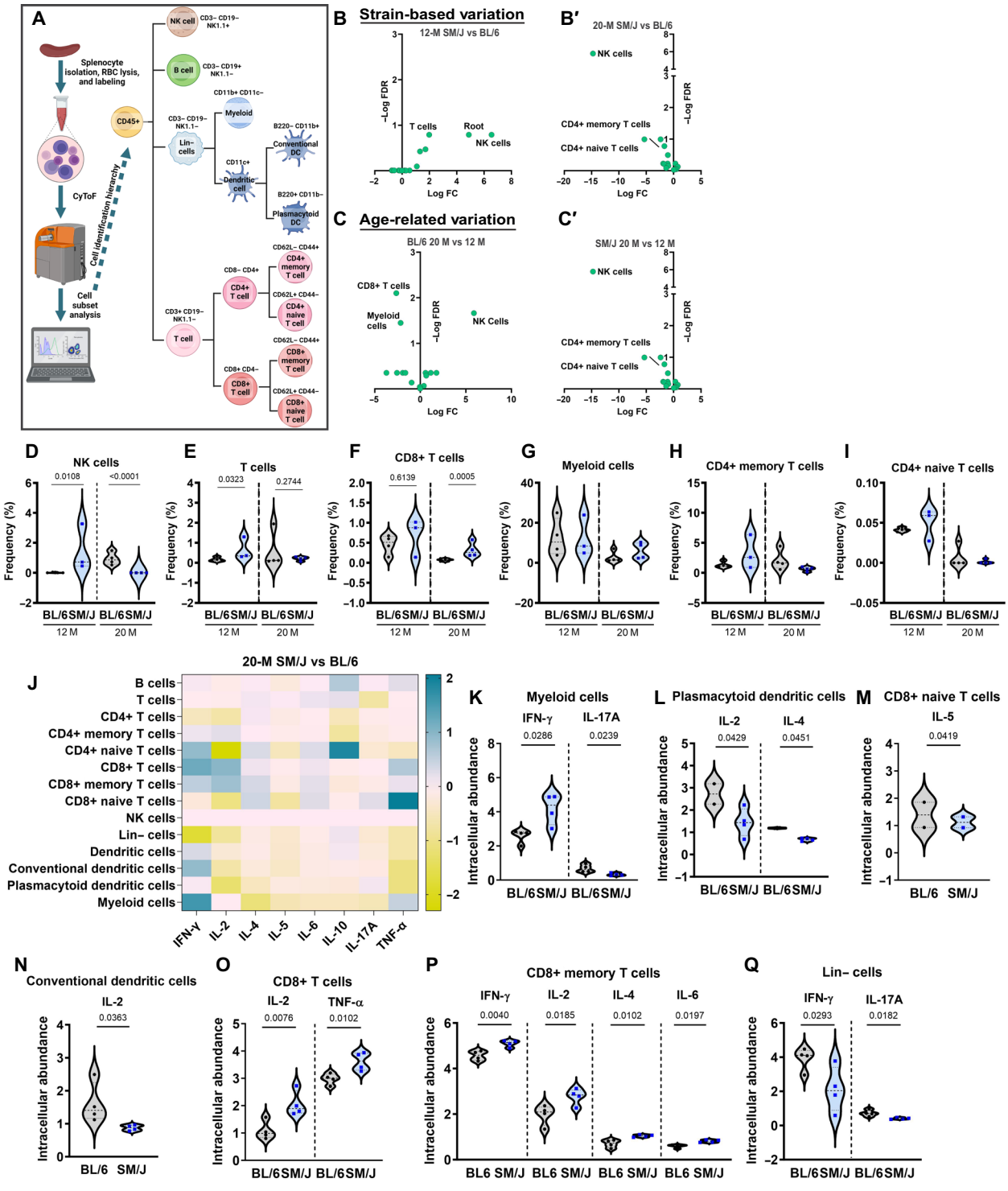

Fig. 7. CyTOF analysis of splenocytes reveals age- and strain-based frequency differences in immune cell populations, and intracellular marker abundance in 20-M SM/J splenocytes indicates possible repression of the innate immune system and overactivation of CD8+ T cell populations. (**A**) Schematic showing the workflow for CyTOF analysis of splenocytes from BL/6 and SM/J mice and the cell population labeling hierarchy. $n_{12\,M\,BL/6} = 2$ females and 2 males; $n_{12\,M\,SM/J} = 2$ females and 1 male; $n_{20\,M\,BL/6} = 2$ females and 2 males; $n_{20\,M\,SM/J} = 4$ males. DC, dendritic cell. (**B** to **C′**) Volcano plots showing cell populations in strain- and age-based comparisons based on FDR and FC. (**D** to **I**) Frequency plots showing age- or strain-based differences in (D) NK cell, (E) T cell, (F) CD8+ T cell, (G) myeloid cell, (H) CD4+ memory T cell, and (I) CD4+ naïve T cell populations. (**J**) Heatmap of splenocytes from 20-M SM/J versus BL/6 showing intracellular cytokine and pro-inflammatory marker abundance within each cell population identified through CyTOF analysis. (**K** to **Q**) Significant changes in cytokine/pro-inflammatory marker abundance in (K) myeloid cells, (L) conventional dendritic cells, (M) plasmacytoid dendritic cells, (N) Lin− cells, (O) CD8+ naïve T cells, (P) CD8+ T cells, and (Q) CD8+ memory T cells. Two-tailed *t* test or Mann-Whitney test was used as appropriate.

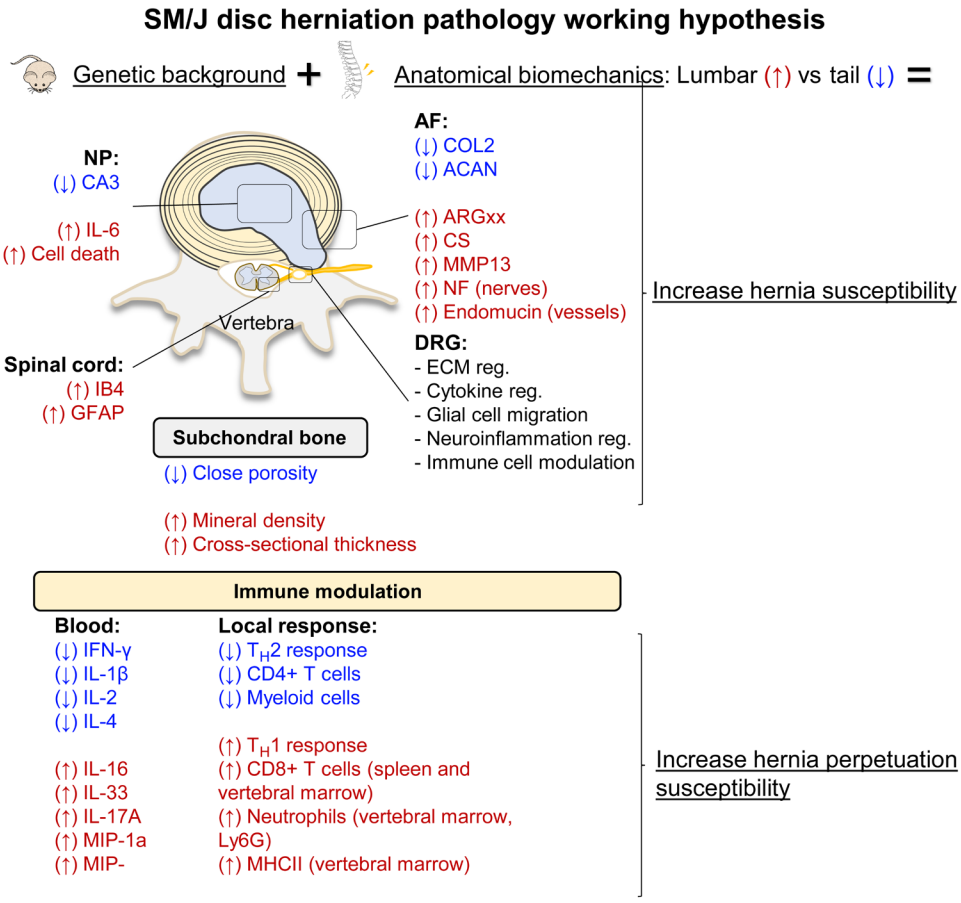

Fig. 8. Summary schematic describing the SM/J herniation phenotype. Working hypothesis and phenotypic changes found in the NP, AF, subchondral bone, DRGs, spinal cord, plasma, and immune tissues of SM/J mice relevant to herniation and chronic pain–related behaviors.

suggested that disc herniation occurs more from end-plate junction failure than AF rupture. While there is a limited ability to assess AF rupture versus end-plate failure in SM/J, and SM/J mice may be a more severe herniation case than the average human patient, this model successfully mimics the human phenotype in the sense that SM/J herniation is not induced by acute injury or single-gene manipulation, as has historically been the case in mouse models of disc herniation.

Considering that the ECM plays a critical role in disc function, the lack of age-associated thickening of collagen fibers in SM/J suggested diminished remodeling of the AF, possibly due to low cell density (*49*). On the other hand, an increased abundance of MMP13 and ARGxx and decreased ACAN with increased CS levels suggested the breakdown of the aggrecan-rich matrix in SM/J mice, with possible compensatory efforts by other sulfated proteoglycans, such as versican (*50*). This loss of ECM integrity likely causes loss of disc structural integrity and mechanical properties (*19*). Notably, ACAN levels and turnover directly modulate axonal ingrowth and pain in degenerated human discs and arthritis models (*51*, *52*). In addition, the increased CS levels in the inner AF of SM/J mice may result in a loss of demarcation between the NP and AF and increased transition zone instability, further exacerbated by reduced abundance of COL2, promoting AF weakness and consequently increasing susceptibility to herniation (*53*). Furthermore, reduced ACAN and CS levels with aging are likely an important contributor to a higher propensity for peripheral nerve ingrowth in herniated SM/J discs (*54*, *55*). When AF DEGs from 12-M SM/J were cross referenced with those from humans susceptible to disc herniation, we observed a down-regulation of ECM-related transcripts, further supporting a key role of ECM homeostasis in preventing herniations and previous findings showing fewer, thinner, and more disorganized collagen I fibers in human herniated discs (*8*, *10*, *56*).

Comparing SM/J findings to those of degenerated human AF (*57*, *58*) showed that dysregulation in cell cycle, cell viability, extracellular structure, and neutrophil activation pathways was shared between the two species. Previous studies have indicated the importance of the immune system in tissue healing after herniation (*59*), and while the disc compartment is immune privileged (*49*), our results suggest that dysregulation of local innate immune response may precede acute herniation and prevent efficient resorption of the herniated mass and scar tissue formation. Similarly, human TNF-α transgenic mice showed higher susceptibility to disc herniation associated with compromised AF integrity and local alterations in immune cell recruitment (*10*, *60*). Notably, despite higher vertebral osteopenia in old SM/J (*4*), these mice show higher subchondral bone thickening. These results align with earlier observations, wherein an aberrant increase in subchondral bone volume/thickness in lumbar vertebrae and knee joints promoted by osteoclastic secretion of netrin-1 induces sensory innervation and pain (*14*, *24*).

cLBP is the primary clinical symptom associated with disc herniations (*61*). In addition, patients often experience radiating pain in their limbs, increased sensitization to mechanical and thermal stimuli, and altered gait (*61*)—phenotypes we noted in aged SM/J mice. Before our investigation, the only behavioral study of SM/J mice evaluated depression-like behavior in 4- and 8-week-old animals and showed a lower response during tail suspension and forced swim tests (*62*, *63*). While our studies did not investigate depression as a possible contributor to pain, it is critical to note that the prior studies on depression in SM/J mice evaluated juvenile mice, as opposed to aged mice, and in the present study, SM/J mice with pain behaviors did not display other indicators of depression, such as fasting, weight loss, or altered grooming (*4*, *64*). Some studies in the literature suggest a sex-dependent influence on disc degeneration and back pain (*65*). However, in our current study, we did not observe a significant impact of sex on the degenerative phenotypes. This may be attributed to the stronger influence of genetic background, which could overshadow any potential sex-related effects.

Notably, while we cannot completely exclude a possible contribution of degeneration of other joints, namely ankle, knee, and hip, in our behavioral findings, these pathologies usually display a longer swing phase, slower swing speed, and decreased paw area in gait analysis, which we did not observe in our cohorts. Together with the changes observed in the lumbar region, but not at the thoracic region of the spinal cord, which corresponded to the lumbar levels of disc hernias and behavioral changes (leg innervation region), our data suggest a higher contribution of the spine phenotype to the neuropathic behavior. As in humans, the ideal method to characterize disc herniation is by magnetic resonance imaging studies; while this was not feasible, by performing sequential transverse and coronal sections, we were able to capture the herniated tissue through AF, speculating that in the most severe case, this herniated material may ingress into the foramen or the spinal canal, promoting local inflation, culminating in the behavioral changes we observed in our study.

Mechanistically, degenerated SM/J discs had higher levels of IL-6, also noted in disc puncture models and osteoarthritis (*66*, *67*), which serves as a chemoattractant for axonal ingression, promoting local neuropathic pain (*68*). Accordingly, increased vascular and sensory innervations were observed in the outer AF but, unlike other studies, not in the NP of herniated SM/J discs (*69*). This finding may be explained by hernia remodeling stages: acute versus absorbed versus chronic (*5*, *10*). In humans, herniated discs show the presence of CGRP- and IB4-positive nociceptive neurons (*25*) and an overall higher percentage of CGRP-positive peptidergic axons (*25*). In addition, increased local IL-6 can, directly and indirectly, modulate responses in surrounding tissues, sensitizing the segmental DRGs and further perpetuating pain (*68*). In both acute and chronic pain models, ECM modulation in the DRGs correlates with pain (*70*). MMPs, including MMP2 and MMP9, which break down ECM, can interact with cytokines and integrins, reducing the local capacity for peripheral nerve regeneration, neuroplasticity, and connectivity and potentially contributing to neuropathy and chronic pain (*71*). Moreover, astrocytes interact with the ECM by expressing several matrix components, such as hyaluronan, or proliferate in response to local fibronectin signaling (*72*, *73*). In agreement with this idea, we observed a concomitant modulation of astrocyte and matrix pathways in SM/J DRGs, with up-regulated DEGs linked to microglial migration, perception of pain signaling, regulation of neuron death, and neuroinflammatory response pathways.

The spinal cord conducts pain-stimulated signals through the central nervous system to the regions of the brain (*74*). We observed a higher abundance of IB4+ axons, a nociceptive neuronal marker, in the dorsal horn of SM/J. In addition, we noted increased GFAP and changes in astrocyte distribution in the deeper layers of the tissue. While higher levels of GFAP are associated with increased pain, it was unexpected to observe an age-associated change in the number and distribution of astrocytes in the dorsal horn in both BL/6 and SM/J strains (*31*). Expression of pain-associated markers was restricted to the lumbar region of the spinal cord, with no differences observed in the thoracic region. Coalescence of disc herniation, DRG, and spinal cord changes in the lumbar spine of aged SM/J mice supports the hypothesis of a discogenic pain source in these animals.

Transcriptomic studies of the DRGs additionally highlighted the associations between discogenic sensitization, inflammatory cytokine modulation, and local immune system regulation, associations that are well accepted (*75*). We explored the cross-talk between changes in the DRGs and systemic inflammation, as aging and senescence are associated with increased systemic inflammation, reduced immune activity and efficiency, and increased prevalence of musculoskeletal diseases and neuropathic pain (*67*, *76*, *77*). Several cytokines, such as IL-1, IL-10, IFN-γ, and TNF-α, have been associated with disc pathology (*78*), with TNF-α and IL-1 playing prominent roles in disc herniation and homeostasis (*79*). Our results showed a negative correlation between mechanical allodynia and systemic IFN-γ, IL-1, IL-2, and IL-4 levels. Considering that an insufficient and distorted immune response can limit hernia resorption and healing, these results align well with the histological evidence of unresolved herniations in aged SM/J mice. Noteworthily, local changes in several interleukins (IL-1, IL-2, IL-4, IL-6, IL-8, IL-10, IL-12, and IL-17) as well as IFN-γ regulation were observed in DRGs from aged SM/J mice, furthering the parallels between systemic and local inflammatory cytokines, immune regulation, and discogenic sensitization (*75*). In addition, we found that in the AF and vertebral tissues, T cell activation correlated with persistent hernia. A previous study of herniated human discs described the presence of activated T cells in 17% of the herniated discs (*80*). Building on this framework, we analyzed immune cell profiles in the primary lymphoid organ (spleen) and peripheral circulation, which showed a contraction of the lymphoid compartment at the expense of the myeloid compartment during BL/6 aging, as reported previously (*81*). Our analyses showed an overactivation of CD8+ T cells and inhibition of CD4+ T cells in SM/J mice. These results agree with recent studies attributing a key role to CD4+ subsets, namely regulatory T cell and T_H2, in suppressing pain and CD8+ T cells in chronic pain (*82*, *83*). PBMC analysis suggests a genetic background–based dysregulation of CD4+ and CD8+ cells, as SM/J mice show a unique population of these cell types by 2 years of age. Unexpectedly, while we observed a higher expression of INF-γ in splenic CD8+ T cells, systemic levels showed an inverse correlation with pain. While active CD8+ T cells and myeloid cells express higher INF-γ in the spleen, the systemic levels likely reflect the total decrease in INF-γ in splenic Lin− cells and PBMCs, which showed lower levels of monocytes, NK cells, and T cells. Despite a lower proportion of T cells systemically, GSEA suggested an elevated T cell–driven response in 20-M SM/J, which aligns with findings in patients with chronic pain (*83*, *84*). In line with this, SM/J splenocytes showed as immune response skewing toward T_H1, supported by lower levels of IL-2 and IL-4 (*82*–*84*). Sciatic nerve injury and osteoarthritis pain phenotypes are modulated by B

cell recruitment and B cells expressing Mu opioid receptors (*85*, *86*); notably, SM/J mice also evidence higher proportions of B cells in circulation during aging, and these cells may contribute to pain sensitization associated with herniations. As previous studies reported a vital role of innate immune system quiescence in perpetuating herniation-associated back pain, we observed a significant deficiency of innate response, specifically the monocytes, granulocytes, and NK cells in the peripheral circulation of SM/J (*13*). While we observed an increase of peripheral macrophages in the 20-M SM/J group with herniations, transcriptomic profiles showed a suppressed immune response, suggesting an insufficient immune response and possible sterile inflammation. A recent study specifically investigated disc hernia regression in the context of macrophage depletion and restoration, providing critical evidence of the need for sufficient macrophage activity in resorption (*12*). The possibility of macrophage deficiency promoting sterile inflammation was further supported by our plasma analysis, showing decreased IFN-γ and lower intracellular cytokine abundance in the splenic innate immune cell populations analyzed with CyTOF. Acknowledging the differences in immune regulation between humans and mice, Moss *et al.* (*87*) described a common aging-related macrophage defect that impairs migration and phagocytosis in both species. This finding further supports the concept of immune quiescence and may help explain the higher incidence of disc hernia in the aging population across species. Noteworthily, local increases of IL-6, in addition to systemic decreases of IL-2 and IL-4, are indicative of M1 macrophage polarization, which has been linked to chronic pain (*88*). A previous study has found varying age-related trends in NK cell abundance, hypothesizing that this may reflect the lack of universality in NK cell dynamics during aging (*89*). In the present study, CyTOF and PBMC analyses showed an age-associated reduction of NK cells in SM/J mice, underscoring an additional indicator of dampened innate immunity. Together, these findings highlight a possible cross-talk between increased CD8+ T cell activity and dampening of the innate immune system, driven by a dysregulated T_H1 immune response, failed hernia resorption, and consequently, the resolution of back pain. Future preclinical and clinical studies will be critical in evaluating the relationship between immune signatures and disc herniation.

In summary, our studies describe a novel clinically relevant mouse model of spontaneous, age-associated disc herniation on a wild-type strain background. As in humans, genetic susceptibility plays a profound role in SM/J disc pathology, and SM/J mice evidence several salient features of discogenic chronic pain (Fig. 8A). Despite the observational nature, we can consider SM/J genetic background and age as independent variables and upstream drivers of the multisystem changes observed in the disc, nervous tissue, and immune system. Our studies provide new insights into the molecular pathophysiology of chronic discogenic pain and demonstrate a key role of immune cell dysregulation in both lymphoid organs and peripheral circulation in mediating, and as a predisposing factor to, this process.

METHODS

Mice, treatment, and study design

All animal experiments were performed under Institutional Animal Care and Use Committee protocol 01679 approved by Thomas Jefferson University. Mice were studied at 6 (healthy adult, 6 M), 12 (middle-aged, 12 M), and 20 M of age (aged, 20 M; mice were collected between 18 and 22 M, with an average age of 20 M). C57BL/6 mice were obtained from the rodent colony at the National Institutes of Aging. The SM/J mice were obtained from the Jackson Laboratory (stock no. 000687, Jackson Labs), bred, and aged at Thomas Jefferson University. The terminal point of 18 to 22 M was chosen on the basis of the comparative life phases of C57BL/6J mice and humans (*90*).

Histological analysis

Histological analysis was performed using six lumbar levels from L1-S1: $n_{BL/6\ 6\ M} = 5$ (3 females and 2 males); $n_{BL/6\ 12\ M} = 6$ (2 females and 4 males); $n_{BL/6\ 20\ M} = 9$ (3 females and 6 males); $n_{SM/J\ 6\ M} = 7$ (4 females and 3 males); $n_{SM/J\ 12\ M} = 10$ (6 females and 4 males); $n_{SM/J\ 20\ M} = 8$ (2 females and 6 males). At terminal time points, mice were either euthanized with CO_2 asphyxiation or anesthetized with ketamine followed by transcardiac perfusion with 0.9% saline, followed by 4% paraformaldehyde (PFA). Lumbar spines were dissected and fixed in 4% PFA in phosphate-buffered saline (PBS) for 6 to 48 hours, decalcified in 20% EDTA, and embedded in optimal cutting temperature compound (OCT) or paraffin. Histological assessment was performed using 10-μm frozen or 7-μm paraffin-embedded midcoronal sections from six lumbar levels (L1-S1). The spinal cord (thoracic and lumbar) and DRGs (lumbar) were harvested from PFA-perfused animals, cryoprotected in 30% sucrose for 3 days, and embedded in OCT. These tissue blocks were cut serially in the sagittal planes at a thickness of 30 μm. Sections were collected on glass slides and stored at −20°C until analysis. Safranin-O/fast green/hematoxylin staining was conducted on six lumbar levels (L1-S1) of each spine. Picrosirius red staining was used to visualize the collagen fibers within the disc. Staining was visualized using an Axio Imager 2 microscope (Carl Zeiss) using 5×/0.15 N-Achroplan or 20×/0.5 EC Plan-Neofluar objectives (Carl Zeiss) or a polarizing light microscope (Eclipse LV100 POL; Nikon, Tokyo, Japan). Four blinded observers scored midcoronal sections from six lumbar discs per mouse using a modified Thompson grading scale (*19*).

Immunohistology and cell number measurements

Following antigen retrieval, deparaffinized sections were blocked in 5% normal serum in PBS with Tween 20 and incubated with antibodies against COL2 (1:400, Fitzgerald, 70R-CR008), COMP (1:200, Abcam, ab231977), CS (1:300, Abcam, ab11570), CA3 (1:150, Santa Cruz), IL-6 (1:50, Novus, NB600-1131), and MMP13 (1:150, Abcam, ab39012). A MOM kit (Vector Laboratories, BMK-2202) was used for blocking and primary antibody incubation for ARGxx (1:200, Abcam, ab3773) staining. Tissue sections were washed and incubated with species-appropriate Alexa Fluor 594–conjugated secondary antibodies (Jackson ImmunoResearch Lab Inc., 1:700). Sections were mounted with ProLong Diamond Antifade Mountant with 4′,6-diamidino-2-phenylindole (DAPI; Thermo Fisher Scientific, P36971) and visualized with an Axio Imager 2 microscope using 5×/0.15 N-Achroplan or 20×/0.5 EC Plan-Neofluar objectives, and images were captured with an Axiocam MRm monochromatic camera (Carl Zeiss). Staining area and cell number quantification was performed using ImageJ software version 1.53e (last access: 6 September 2020; http://rsb.info.nih.gov/ij/) (*91*).

Slides with spinal cord sections were first warmed for 1 hour at 37°C before three 5-min washes in PBS to remove OCT medium. Slides were then blocked for 1 hour in blocking buffer (5% Donkey Serum and 0.1% Triton X-100 in PBS) and then incubated at 4°C overnight with primary antibodies against Iba1 (1:600, WAKO,

AB_839504) and GFAP (1:400, Dako, Carpinteria, CA; AB_10013482) diluted in blocking buffer. Slides were then washed and incubated in the appropriate secondary antibody (1:200, Donkey anti-Rabbit Alexa Fluor 647, AB_2492288, or Donkey anti-rabbit Alexa Fluor 488, AB_2313584, in blocking buffer) before being mounted with Fluorsave (Millipore Sigma) and imaged.

Neuronal, vascular, and immune staining in the spinal column

Endomucin (1:300, Santa Cruz Biotechnology, sc-65495), neurofilament (1:200, BioLegend, 837904), IB4 (1:200, Sigma-Aldrich, L2895), CGRP (1:50, Abcam, ab36001), IB4 (1:200, Sigma-Aldrich, L2895), CD19 (1:50, BioLegend, 115569), CD3 (1:50, BioLegend, 100202), Ly6G (1:50, BioLegend, 127602), MHCII (1:50, Thermo Fisher Scientific, 50-112-9377), and F4/80 (1:50, Cell Signaling, 70076S) stains were imaged on a Zeiss LSM 800 equipped with a Plan Apochromat 20×, 0.8–numerical aperture air objective (Zeiss). Wavelength excitation was 488, 594, 647, or 405 nm based on antibody conjugates, and samples were captured as tiled or untiled *z*-stacks at a 1.0-μm interval. Tiled images were oriented to an upright angle and cropped to 1024 by 1024, and brightness and contrast were linearly adjusted using ImageJ 1.52i (National Institute of Health).

TUNEL assay

Cell viability staining was performed using the in situ cell death detection kit (Roche Diagnostic). In summary, sections were deparaffinized and permeabilized using proteinase K (20 μg/ml) for 15 min, and the TUNEL assay was carried out per the manufacturer's protocol. Sections were washed and mounted with ProLong Diamond Antifade Mountant with DAPI and visualized and imaged with the Axio Imager 2 microscope.

Digital image analysis

All immunohistochemical quantification was conducted in grayscale using the Fiji package of ImageJ (*91*). Images underwent thresholding to create binary images, and NP, AF, end-plate (EP), or vertebral compartments were manually defined using the Freehand Tool. These defined regions of interest were then analyzed using either the Analyze Particles (TUNEL and cell number quantification) function or the Area Fraction measurement.

Tissue RNA isolation and microarray analysis

AF tissues were dissected from lumbar discs (L1-S1) of 12- and 20-M-old BL/6 and SM/J animals [$n_{\text{BL/6 12 M}} = 5$ (5 males); $n_{\text{BL/6 20 M}} = 4$ (3 females and 1 male); $n_{\text{SM/J 12 M}} = 4$ (4 males); $n_{\text{SM/J 20 M}} = 4$ (2 females and 2 males)]. Eight to 10 DRGs were collected from the lumbar region (L1-S1) from 12- and 20-M BL/6 and SM/J mice (three males and three females per strain per time point). Pooled tissue from a single animal served as an individual sample. Samples were homogenized, and total DNA-free RNA was extracted using the RNeasy Mini kit (Qiagen).

Total RNA with an RNA integrity number >4 was used for microarray analysis. Fragmented biotin-labeled cDNA was synthesized using the GeneChip WT Plus kit (Thermo Fisher Scientific). Gene chips (Mouse Clariom S) were hybridized with biotin-labeled cDNA. Arrays were washed and stained with the GeneChip hybridization wash & stain kit and scanned on an Affymetrix Gene Chip Scanner 3000 7G. Quality control of the experiment was performed in Expression Console Software version 1.4.1.. CHP files were generated by sst-rma normalization from Affymetrix.CEL files using Expression Console Software. Only protein-coding genes were included in the analyses. Detection above background higher than 50% was used for significance analysis of microarrays, and the FDR value was set at 5% and FC ≥ 2. Biological process enrichment analysis was performed using the PANTHER Overrepresentation Test with Panther GO Slim Biological Processes and Panther Pathway database annotations and a binomial statistical test with FDR ≤ 0.05. Analyses and visualizations were conducted in Affymetrix Transcriptome Analysis Console 4.0 software. Pathway schematic analyses were performed using the Transcriptome Analysis Console. Array data are deposited in the Gene Expression Omnibus (GEO) database (GSE252383).

Human microarray analysis

Human AF transcriptomic analysis was performed with the GSE70362 dataset available in the GEO database by Kazezian *et al.* (*23*). First, degenerative and healthy clusters were obtained by hierarchical clustering of DEGs using Euclidean metrics. Human AF samples with Thompson grades I and II were grouped into a healthy category, those with grades III and IV were considered degenerated, and those with grade V were considered herniated. To maintain consistency between human and mouse samples, healthy versus degenerated was compared with 1-year SM/J and BL/6 samples and herniated versus healthy and degenerated compared against SM/J 20-M aging DEGs, obtained with $P \leq 0.05$ and FC ≥ 1.3 for healthy versus degeneration comparison and $P \leq 0.05$ for herniation versus healthy and degeneration. For human and mouse comparison, both human and mouse DEGs were first mapped using Panther generic mapping from reference proteome genome organisms and then overlapped to identify the common DEGs between each group. To study the biological pathways commonly modulated between humans and mice (independent of specific genes), we used theme/concept analysis using the CompBio tool (PercayAI Inc., St. Louis, MO) ($P \leq 0.05$; table S2) (*92*).

Plasma cytokine analysis

Blood was collected by intracardiac puncture in heparin-coated syringes and centrifuged at 1500 relative centrifugal force (rcf) at 4°C for 15 min to isolate the plasma. Samples were stored at −80°C until the time of analysis. According to the manufacturer's specifications, levels of pro-inflammatory proteins, cytokines, and T_H17 mediators were analyzed using the V-PLEX Mouse Cytokine 29-Plex Kit (Meso Scale Diagnostics, Rockville, MD).

Behavior testing

Modified versions of the Hargreaves, cold stimulus, and von Frey filament tests were used to measure heat, cold, and mechanical sensitivity, respectively (*28*, *29*). Hind paw withdrawal for Hargreaves, cold, and von Frey tests was defined by removing the paw from the infrared, dry ice (through a glass plate), or mechanical stimulus. All scored withdrawal responses were associated with one or more supraspinal responses, including vocalization and licking and/or guarding of the tested paw. Spontaneous movements were not recorded, and each trial was conducted in triplicate. Cutoffs of 30 s for the Hargreaves and cold stimuli tests and 2 g of force for the von Frey test were used to prevent damage to the animal's paw.

Subchondral bone microcomputed tomography analysis

Lumbar spines were dissected from 20-M C57BL/6J and SM/J mice [$n_{BL/6} = 5$ (2 females and 3 males); $n_{SM/J} = 5$ (3 females and 2 males)], fixed in 4% PFA for 48 hours, and rehydrated with 1× PBS for assessment with the SkyScan 1275 μCT imaging system (Bruker). Scanning settings were 200-μA current, 50-kV voltage, and 15 μm per pixel. The skeletal parameters assessed by microcomputed tomography followed previously published nomenclature guidelines (*93*). Images were reconstructed through NRecon (Bruker) before analysis in CTAn (Bruker). The regions of interest were limited to subchondral bone and end plate by selecting five cross-sectional slices, which excluded extraneous trabeculae of the vertebral body. The density of mineralized tissue was obtained through CTAn using appropriate thresholding. Subsequent two-dimensional analysis was used to assess bone volume (BV), mean bone area of selected cross sections (B.Ar), cross-sectional thickness (Cs.Th), bone surface fraction (BS/BV), and closed porosity (*93*).

PBMC single-cell preparation and sequencing

Whole blood was collected from 12- and 20-M SM/J and BL/6 mice ($n_{12\,M\,BL/6} = 2$ females and 2 males; $n_{12\,M\,SM/J} = 2$ females and 1 male; $n_{20\,M\,BL/6} = 2$ females and 2 males; $n_{20\,M\,SM/J} = 4$ males) via intracardiac puncture and diluted into an equal volume of Dulbecco's PBS and 2% fetal bovine serum (FBS; StemCell Technologies, 07905). According to the manufacturer's specifications, blood was layered on top of Lymphoprep (StemCell Technologies, 07851) in a 15-ml tube and centrifuged at 800 rcf for 20 min at room temperature. The mononuclear cells were washed twice with PBS + 2% FBS, and platelets were removed with an additional centrifugation at 120 rcf for 10 min. To facilitate the removal of any remaining red blood cells (RBCs), a lysis step was performed (BioLegend, 420302). Briefly, lysis buffer (1×) was added to the cell suspension and incubated for 5 min, with periodic inversion. Cells were then centrifuged at 350 rcf for 10 min, and PBMCs were washed twice with PBS + 2% FBS. Cell suspensions were processed for scRNA-seq using the 10X Genomics 3' version 3 kit (10x Genomics, Pleasanton, CA), with interstrain multiplexing, according to the manufacturer's specifications. Sequencing was performed with Illumina NextSeq 2000 according to the manufacturer's instructions (Illumina).

scRNA-seq data analysis

Raw data were aligned to the mouse reference transcriptome (mm10-2020-A) and underwent preprocessing with Cell Ranger Multi version 7.0.1. According to the authors' recommended workflow, the count matrix was analyzed using Seurat version 4.3.0 (*94*). Briefly, data were converted into Seurat Objects using the CreateSeuratObject function, and all cells were analyzed for their unique molecular identifier and mitochondrial gene fractions; cells were included if $200 < n_{feat} < 2500$, and mitochondrial genes accounted for <5%. Data were integrated with logarithmic normalization (LogNormalize) and organized according to variation in the data using FindVariableFeatures. Dimensional reduction was performed using principal components analysis, and the FindNeighbors (dims = 1:15) function, followed by the FindClusters functions, was used to calculate the number of cell clusters using the Louvain algorithm, with the resolution parameter set to 0.5. DimPlot was then used to visualize the data as UMAP. Cell types for each age and strain condition were determined using SingleR, with the MouseRNAseqData reference dataset and main labels (*33*). Individual cell types were individually subset and analyzed via the same methodology to determine strain- and age-based variation within each cell type, with DEG results in table S3. The clusterProfiler package was used to conduct GSEA on DEGs (FDR < 0.05) identified in various strain- and age-based comparisons (*36*). Data are deposited and may be accessed in the GEO database (GSE252474), and relevant R scripts can be found at https://github.com/mrisbudlab or https://datadryad.org/stash/share/UIzO6e_x3uLqiw3zPr0Zv0ntHbXZPrXP-hG02aA5Iec.

Splenocyte preparation and CyToF

Spleens were collected from 12- and 20-M SM/J and BL/6 mice ($n_{12\,M\,BL/6} = 2$ females and 2 males; $n_{12\,M\,SM/J} = 2$ females and 1 male; $n_{20\,M\,BL/6} = 2$ females and 2 males; $n_{20\,M\,SM/J} = 4$ males). Splenocytes were dissociated from the tissue matrix by gentle compression through a 100-μm strainer (StemCell Technologies, 27217). RBC lysis (BioLegend, 420302) was performed, followed by two PBS + 3% FBS washes. Cells were then resuspended in complete medium (Sigma-Aldrich, D6046) + 10% FBS (Sigma-Aldrich, F2442) + 2% 50× penicillin/streptomycin (Corning, 30-001-CI) at a concentration of 1×10^6 cells/ml. To stimulate intracellular cytokine production, Cell Activation Cocktail (2 μl/ml) with Brefeldin A (BioLegend, 423303) was incubated with the cells at 37°C for 4 hours. After incubation, the mixture was washed twice in serum-free media and resuspended in serum-free media at a concentration of 2×10^7 cells/ml. To label dead cells, Cell-ID Cisplatin (Standard Biotools, 201064) was added to each cell suspension at a concentration of 10 μM. Cell staining according to the manufacturer's protocol for the Maxpar Mouse Sp/LN Phenotyping Panel Kit (16 markers: Ly6G/C[Gr1], CD11c, CD69, CD45, CD11B[MAC1], CD19, CD25, CD3e, TER-110, CD62L, CD8a, TCRI^2, NK1.1, CD44, CD4, and B220) (Standard Biotools, 201306) was carried out for all samples. 18-M SM/J and BL/6 splenocytes underwent a subsequent round of staining according to the manufacturer's specs for the Maxpar Mouse Intracellular Cytokine I Panel Kit (eight markers: IFN-γ, IL-2, IL-4, IL-5, IL-6, IL-10, IL-17A, and TNF-α) (Standard Biotools, 201310). After all staining, samples were washed, fixed with 1.6% PFA in PBS, and incubated with Cell-ID Intercalator-Ir, per the Maxpar staining protocols. After this incubation, cells were washed once, passed through a 100-μm cell strainer, and resuspended in freezing media composed of 90% FBS + 10% dimethyl sulfoxide. Cells were stored at −80°C until the time of analysis. Cells were quickly thawed at 37°C and washed three times in CAS buffer at 800*g* for 10 min. Cells were resuspended at 1×10^6/ml in CAS buffer and strained through a 35-μm filter before acquisition. Each sample was acquired on a CyTOF 2 Helios mass cytometer.

CyToF analysis

Single-cell data have been clustered using the FlowSOM R package and labeled using the Ek'Balam algorithm (*95*, *96*). Cell subset definitions follow guidelines by Maecker *et al.* (*97*) and Finak *et al.* (*98*). Cluster labeling, method implementation, and visualization were conducted through the Astrolabe Cytometry Platform (Astrolabe Diagnostics Inc.). The Astrolabe Mass Cytometry Platform is a cloud-based service for analyzing mass cytometry data. Astrolabe labels events into immune subsets in a two-stage process. First, events are clustered using self-organizing maps implemented by the FlowSOM package. Clusters are then labeled, following a manually curated gating hierarchy. Multidimensional scaling maps were generated using the cmdscale R function (*99*). Differential abundance

analysis was done using the edgeR package (*100*) following the methods outlined by Lun *et al.* (*101*). Differential expression analysis was done using the limma R package (*102*) followed by diffcyt (*103*).

Statistical analyses

All statistical analyses were performed using Prism7 (GraphPad, La Jolla). Data distribution was assessed with the Shapiro-Wilk normality test, and the differences between the two groups were analyzed by *t* test or Mann-Whitney test, as appropriate. Differences between more than two groups were analyzed by analysis of variance (ANOVA) or Kruskal-Wallis test for non-normally distributed data, followed by Dunn's multiple comparison test. Chi-square test was used to analyze the differences between the distributions of percentages. $P \leq 0.05$ was considered a statistically significant difference.

Supplementary Materials

The PDF file includes:
Figs. S1 to S17
Legends for tables S1 to S3

Other Supplementary Material for this manuscript includes the following:
Tables S1 to S3

REFERENCES AND NOTES

1. GBD 2017 Disease and Injury Incidence and Prevalence Collaborators, Global, regional, and national incidence, prevalence, and years lived with disability for 354 diseases and injuries for 195 countries and territories, 1990–2017: A systematic analysis for the Global Burden of Disease Study 2017. *Lancet* **392**, 1789–1858 (2018).
2. J. N. Katz, Lumbar disc disorders and low-back pain: Socioeconomic factors and consequences. *J. Bone Joint Surg. Am.* **88**, 21–24 (2006).
3. K. M. C. Cheung, J. Karppinen, D. Chan, D. W. H. Ho, Y.-Q. Song, P. Sham, K. S. E. Cheah, J. C. Y. Leong, K. D. K. Luk, Prevalence and pattern of lumbar magnetic resonance imaging changes in a population study of one thousand forty-three individuals. *Spine* **34**, 934–940 (2009).
4. E. J. Novais, V. A. Tran, J. Miao, K. Slaver, A. Sinensky, N. A. Dyment, S. Addya, F. Szeri, K. van de Wetering, I. M. Shapiro, M. V. Risbud, Comparison of inbred mouse strains shows diverse phenotypic outcomes of intervertebral disc aging. *Aging Cell* **19**, e13148 (2020).
5. S. Tessier, V. A. Tran, O. K. Ottone, E. J. Novais, A. Doolittle, M. J. Di Muzio, I. M. Shapiro, M. V. Risbud, TonEBP-deficiency accelerates intervertebral disc degeneration underscored by matrix remodeling, cytoskeletal rearrangements, and changes in proinflammatory gene expression. *Matrix Biol.* **87**, 94–111 (2019).
6. M. Tsingas, O. K. Ottone, A. Haseeb, R. A. Barve, I. M. Shapiro, V. Lefebvre, M. V. Risbud, Sox9 deletion causes severe intervertebral disc degeneration characterized by apoptosis, matrix remodeling, and compartment-specific transcriptomic changes. *Matrix Biol.* **94**, 110–133 (2020).
7. F. Yang, V. Y. L. Leung, K. D. K. Luk, D. Chan, K. M. C. Cheung, Injury-induced sequential transformation of notochordal nucleus pulposus to chondrogenic and fibrocartilaginous phenotype in the mouse. *J. Pathol.* **218**, 113–121 (2009).
8. H. E. Gruber, E. H. Sage, H. J. Norton, S. Funk, J. Ingram, E. N. Hanley Jr., Targeted deletion of the SPARC gene accelerates disc degeneration in the aging mouse. *J. Histochem. Cytochem.* **53**, 1131–1138 (2005).
9. M. Millecamps, M. Tajerian, E. H. Sage, L. S. Stone, Behavioral signs of chronic back pain in the SPARC-null mouse. *Spine* **36**, 95–102 (2011).
10. D. J. Gorth, I. M. Shapiro, M. V. Risbud, Transgenic mice overexpressing human TNF-α experience early onset spontaneous intervertebral disc herniation in the absence of overt degeneration. *Cell Death Dis.* **10**, 7 (2018).
11. P. Yu, F. Mao, J. Chen, X. Ma, Y. Dai, G. Liu, F. Dai, J. Liu, Characteristics and mechanisms of resorption in lumbar disc herniation. *Arthritis Res. Ther.* **24**, 205 (2022).
12. C. Ribeiro-Machado, S. G. Santos, I. A. Amaral, J. Caldeira, P. Pereira, M. A. Barbosa, C. Cunha, Macrophage-based therapy for intervertebral disc herniation: Preclinical proof-of-concept. *NPJ Regen. Med.* **8**, 34 (2023).
13. M. Parisien, L. V. Lima, C. Dagostino, N. El-Hachem, G. L. Drury, A. V. Grant, J. Huising, V. Verma, C. B. Meloto, J. R. Silva, G. G. S. Dutra, T. Markova, H. Dang, P. A. Tessier, G. D. Slade, A. G. Nackley, N. Ghasemlou, J. S. Mogil, M. Allegri, L. Diatchenko, Acute inflammatory response via neutrophil activation protects against the development of chronic pain. *Sci. Transl. Med.* **14**, eabj9954 (2022).
14. S. Zhu, J. Zhu, G. Zhen, Y. Hu, S. An, Y. Li, Q. Zheng, Z. Chen, Y. Yang, M. Wan, R. L. Skolasky, Y. Cao, T. Wu, B. Gao, M. Yang, M. Gao, J. Kuliwaba, S. Ni, L. Wang, C. Wu, D. Findlay, H. K. Eltzschig, H. W. Ouyang, J. Crane, F. Q. Zhou, Y. Guan, X. Dong, X. Cao, Subchondral bone osteoclasts induce sensory innervation and osteoarthritis pain. *J. Clin. Invest.* **129**, 1076–1093 (2019).
15. A. L. A. Binch, A. A. Cole, L. M. Breakwell, A. L. R. Michael, N. Chiverton, L. B. Creemers, A. K. Cross, C. L. Le Maitre, Nerves are more abundant than blood vessels in the degenerate human intervertebral disc. *Arthritis Res. Ther.* **21**, 370 (2015).
16. J. Ferreira-Gomes, S. Adães, J. Sarkander, J. M. Castro-Lopes, Phenotypic alterations of neurons that innervate osteoarthritic joints in rats. *Arthritis Rheum.* **62**, 3677–3685 (2010).
17. M. Tsuda, K. Koga, T. Chen, M. Zhuo, Neuronal and microglial mechanisms for neuropathic pain in the spinal dorsal horn and anterior cingulate cortex. *J. Neurochem.* **141**, 486–498 (2017).
18. R.-R. Ji, A. Nackley, Y. Huh, N. Terrando, W. Maixner, Neuroinflammation and central sensitization in chronic and widespread pain. *Anesthesiology* **129**, 343–366 (2018).
19. H. Choi, S. Tessier, E. S. Silagi, R. Kyada, F. Yousefi, N. Pleshko, I. M. Shapiro, M. V. Risbud, A novel mouse model of intervertebral disc degeneration shows altered cell fate and matrix homeostasis. *Matrix Biol.* **70**, 102–122 (2018).
20. Y. Zhang, C. Xiong, M. Kudelko, Y. Li, C. Wang, Y. L. Wong, V. Tam, M. F. Rai, J. Cheverud, H. A. Lawson, L. Sandell, W. C. W. Chan, K. S. E. Cheah, P. C. Sham, D. Chan, Early onset of disc degeneration in SM/J mice is associated with changes in ion transport systems and fibrotic events. *Matrix Biol.* **70**, 123–139 (2018).
21. M. C. Battié, T. Videman, J. Kaprio, L. E. Gibbons, K. Gill, H. Manninen, J. Saarela, L. Peltonen, The Twin Spine Study: Contributions to a changing view of disc degeneration. *Spine J.* **9**, 47–59 (2009).
22. T. Ohnishi, E. J. Novais, M. V. Risbud, Alterations in ECM signature underscore multiple sub-phenotypes of intervertebral disc degeneration. *Matrix Biol. Plus* **6–7**, 100036 (2020).
23. Z. Kazezian, R. Gawri, L. Haglund, J. Ouellet, F. Mwale, F. Tarrant, P. O'gaora, A. Pandit, M. Alini, S. Grad, Gene expression profiling identifies interferon signalling molecules and IGFBP3 in human degenerative annulus fibrosus. *Sci. Rep.* **5**, 15662 (2015).
24. S. Ni, Z. Ling, X. Wang, Y. Cao, T. Wu, R. Deng, J. L. Crane, R. Skolasky, S. Demehri, G. Zhen, A. Jain, P. Wu, D. Pan, B. Hu, X. Lyu, Y. Li, H. Chen, H. Qi, Y. Guan, X. Dong, M. Wan, X. Zou, H. Lu, J. Hu, X. Cao, Sensory innervation in porous endplates by Netrin-1 from osteoclasts mediates PGE2-induced spinal hypersensitivity in mice. *Nat. Commun.* **10**, 5643 (2019).
25. T. Ozawa, S. Ohtori, G. Inoue, Y. Aoki, H. Moriya, K. Takahashi, The degenerated lumbar intervertebral disc is innervated primarily by peptide-containing sensory nerve fibers in humans. *Spine* **31**, 2418–2422 (2006).
26. N. H. Al Nezari, A. G. Schneiders, P. A. Hendrick, Neurological examination of the peripheral nervous system to diagnose lumbar spinal disc herniation with suspected radiculopathy: A systematic review and meta-analysis. *Spine J.* **13**, 657–674 (2013).
27. E. Hasvik, A. J. Haugen, L. Grøvle, Symptom descriptors and patterns in lumbar radicular pain caused by disc herniation: A 1-year longitudinal cohort study. *BMJ Open* **2**, e065500 (2022).
28. E. V. Brown, A. F. Malik, E. R. Moese, A. F. McElroy, A. C. Lepore, Differential activation of pain circuitry neuron populations in a mouse model of spinal cord injury-induced neuropathic pain. *J. Neurosci.* **42**, 3271–3289 (2022).
29. E. V. Brown, A. Falnikar, N. Heinsinger, L. Cheng, C. E. Andrews, M. DeMarco, A. C. Lepore, Cervical spinal cord injury-induced neuropathic pain in male mice is associated with a persistent pro-inflammatory macrophage/microglial response in the superficial dorsal horn. *Exp. Neurol.* **343**, 113757 (2021).
30. D. H. Vrinten, F. F. T. Hamers, "CatWalk" automated quantitative gait analysis as a novel method to assess mechanical allodynia in the rat; a comparison with von Frey testing. *Pain* **102**, 203–209 (2003).
31. J. L. Watson, T. J. Hala, R. Putatunda, D. Sannie, A. C. Lepore, Persistent at-level thermal hyperalgesia and tactile allodynia accompany chronic neuronal and astrocyte activation in superficial dorsal horn following mouse cervical contusion spinal cord injury. *PLOS ONE* **9**, e109099 (2014).
32. O. K. Ottone, C. Kim, J. A. Collins, M. V. Risbud, The cGAS-STING pathway affects vertebral bone but does not promote intervertebral disc cell senescence or degeneration. *Front. Immunol.* **13**, 882407 (2022).
33. D. Aran, A. P. Looney, L. Liu, E. Wu, V. Fong, A. Hsu, S. Chak, R. P. Naikawadi, P. J. Wolters, A. R. Abate, A. J. Butte, M. Bhattacharya, Reference-based analysis of lung single-cell sequencing reveals a transitional profibrotic macrophage. *Nat. Immunol.* **20**, 163–172 (2019).
34. E. Papalexi, R. Satija, Single-cell RNA sequencing to explore immune cell heterogeneity. *Nat. Rev. Immunol.* **18**, 35–45 (2018).
35. A. Sebastian, N. R. Hum, J. L. McCool, S. P. Wilson, D. K. Murugesh, K. A. Martin, N. D. Rios-Arce, B. Amiri, B. A. Christiansen, G. G. Loots, Single-cell RNA-Seq reveals changes in immune landscape in post-traumatic osteoarthritis. *Front. Immunol.* **13**, 938075 (2022).

36. G. Yu, L.-G. Wang, Y. Han, Q.-Y. He, clusterProfiler: An R package for comparing biological themes among gene clusters. *OMICS* **16**, 284–287 (2012).
37. V. Bronte, M. J. Pittet, The spleen in local and systemic regulation of immunity. *Immunity* **39**, 806–818 (2013).
38. E. P. Blankenhorn, G. Bryan, A. V. Kossenkov, L. D. Clark, X.-M. Zhang, C. Chang, W. Horng, L. S. Pletscher, J. M. Cheverud, L. C. Showe, E. Heber-Katz, Genetic loci that regulate healing and regeneration in LG/J and SM/J mice. *Mamm. Genome* **20**, 720–733 (2009).
39. R. Dammers, P. J. Koehler, Lumbar disc herniation: Level increases with age. *Surg. Neurol.* **58**, 209–212 (2002).
40. G. S. Skaf, C. M. Ayoub, N. T. Domloj, M. J. Turbay, C. El-Zein, M. H. Hourani, Effect of age and lordotic angle on the level of lumbar disc herniation. *Adv. Orthop.* **2011**, 950576 (2011).
41. J. J. Sarver, D. M. Elliott, Mechanical differences between lumbar and tail discs in the mouse. *J. Orthop. Res.* **2311**, 150–155 (2005).
42. J. Brendler, K. Winter, P. Lochhead, A. Schulz, A. M. Ricken, Histological differences between lumbar and tail intervertebral discs in mice. *J. Anat.* **240**, 84–93 (2022).
43. S. Tessier, V. Madhu, Z. I. Johnson, I. M. Shapiro, M. V. Risbud, NFAT5/TonEBP controls early acquisition of notochord phenotypic markers, collagen composition, and sonic hedgehog signaling during mouse intervertebral disc embryogenesis. *Dev. Biol.* **455**, 369–381 (2019).
44. A. L. Hornung, S. S. Rudisill, J. N. Barajas, G. Harada, A. A. Fitch, S. F. Leonard, A. C. Roberts, H. S. An, H. B. Albert, A. Tkachev, D. Samartzis, How does resorption differ among single-level and multilevel lumbar disc herniations? A prospective multi-imaging and clinical phenotype study. *Spine* **49**, 763–771 (2024).
45. D.-K. Kim, C. H. Oh, M. S. Lee, S. H. Yoon, H.-C. Park, C. O. Park, Prevalence of lumbar disc herniation in adolescent males in Seoul, Korea: Prevalence of adolescent LDH in Seoul, Korea. *Korean J. Spine* **8**, 261–266 (2011).
46. A. Sarsılmaz, E. Yencilek, Ü. Özelçi, T. Güzelbey, M. Apaydın, The incidence and most common levels of thoracic degenerative disc pathologies. *Turk. J. Phys. Med. Rehabil.* **64**, 155–161 (2018).
47. G. E. Anyanwu, R. T. Ekwunife, E. C. Iyidobi, C. U. Nwadinigwe, H. C. Ekwedigwe, A. U. Agu, E. O. Agbo, Epidemiology of lumbar disc herniations in adults with low back pain in Enugu, Nigeria. *Int. J. Res. Orthop.* **6**, 1–6 (2019).
48. S. Rajasekaran, N. Bajaj, V. Tubaki, R. M. Kanna, A. P. Shetty, ISSLS Prize Winner: The anatomy of failure in lumbar disc herniation: An in vivo, multimodal, prospective study of 181 subjects. *Spine* **38**, 1491–1500 (2013).
49. J. Bedore, A. Leask, C. A. Séguin, Targeting the extracellular matrix: Matricellular proteins regulate cell–extracellular matrix communication within distinct niches of the intervertebral disc. *Matrix Biol.* **37**, 124–130 (2014).
50. R. Sztrolovics, J. Grover, G. Cs-Szabo, S. Shi, Y. Zhang, J. S. Mort, P. J. Roughley, The characterization of versican and its message in human articular cartilage and intervertebral disc. *J. Orthop. Res.* **20**, 257–266 (2002).
51. W. E. B. Johnson, B. Caterson, S. M. Eisenstein, D. L. Hynds, D. M. Snow, S. Roberts, Human intervertebral disc aggrecan inhibits nerve growth in vitro. *Arthritis Rheum.* **46**, 2658–2664 (2002).
52. I. L. Mohd Isa, S. A. Abbah, M. Kilcoyne, D. Sakai, P. Dockery, D. P. Finn, A. Pandit, Implantation of hyaluronic acid hydrogel prevents the pain phenotype in a rat model of intervertebral disc injury. *Sci. Adv.* **4**, eaaq0597 (2018).
53. B. Farrugia, S. M. Smith, C. C. Shu, J. Melrose, Spatiotemporal expression of 3-B-3(−) and 7-D-4 chondroitin sulfation, tissue remodeling, and attempted repair in an ovine model of intervertebral disc degeneration. *Cartilage* **11**, 234–250 (2019).
54. T. M. Hering, J. A. Beller, C. M. Calulot, D. M. Snow, Contributions of chondroitin sulfate, keratan sulfate and N-linked oligosaccharides to inhibition of neurite outgrowth by Aggrecan. *Biology* **9**, 29 (2020).
55. M. L. Lemons, J. D. Sandy, D. K. Anderson, D. R. Howland, Intact aggrecan and chondroitin sulfate-depleted aggrecan core glycoprotein inhibit axon growth in the adult rat spinal cord. *Exp. Neurol.* **184**, 981–990 (2003).
56. A. L. Castro, C. Ribeiro-Machado, C. M. Oliveira, G. Q. Teixeira, C. Neidlinger-Wilke, P. Pereira, R. Vaz, M. A. Barbosa, R. M. Gonçalves, Fibrotic alterations in human annulus fibrosus correlate with progression of intervertebral disc herniation. *Arthritis Res. Ther.* **24**, 25 (2022).
57. J. C. Iatridis, A. J. Michalek, D. Purmessur, C. L. Korecki, Localized intervertebral disc injury leads to organ level changes in structure, cellularity, and biosynthesis. *Cell. Mol. Bioeng.* **2**, 437–447 (2009).
58. A. A. Espinoza Orías, N. R. Malhotra, D. M. Elliott, Rat disc torsional mechanics: Effect of lumbar and caudal levels and axial compression load. *Spine J.* **9**, 204–209 (2009).
59. C. Cunha, A. J. Silva, P. Pereira, R. Vaz, R. M. Gonçalves, M. A. Barbosa, The inflammatory response in the regression of lumbar disc herniation. *Arthritis Res. Ther.* **24**, 205 (2018).
60. D. J. Gorth, O. K. Ottone, I. M. Shapiro, Differential effect of long-term systemic exposure of TNFα on health of the annulus fibrosus and nucleus pulposus of the intervertebral disc. *J. Bone Miner. Res.* **35**, 725–737 (2019).
61. R. Chou, A. Qaseem, V. Snow, D. Casey, T. J. Cross Jr., P. Shekelle, D. K. Owens, Clinical Efficacy Assessment Subcommittee of the American College of Physicians, American College of Physicians, American Pain Society Low Back Pain Guidelines Panel, Diagnosis and treatment of low back pain: A joint clinical practice guideline from the American College of Physicians and the American Pain Society. *Ann. Intern. Med.* **147**, 478–491 (2007).
62. R. D. Moloney, T. G. Dinan, J. F. Cryan, Strain-dependent variations in visceral sensitivity: Relationship to stress, anxiety and spinal glutamate transporter expression. *Genes Brain Behav.* **14**, 319–329 (2015).
63. B. H. Miller, L. E. Schultz, A. Gulati, A. I. Su, M. T. Pletcher, Phenotypic characterization of a genetically diverse panel of mice for behavioral despair and anxiety. *PLOS ONE* **5**, e14458 (2010).
64. H. Yang, E. L. Hurwitz, J. Li, K. de Luca, P. Tavares, B. Green, S. Haldeman, Bidirectional comorbid associations between back pain and major depression in US adults. *Int. J. Environ. Res. Public Health* **20**, 4217 (2023).
65. G. E. Mosley, M. Wang, P. Nasser, A. Lai, D. A. Charen, B. Zhang, J. C. Iatridis, Males and females exhibit distinct relationships between intervertebral disc degeneration and pain in a rat model. *Sci. Rep.* **10**, 15120 (2020).
66. L. Xu, L. N. Nwosu, J. J. Burston, P. J. Millns, D. R. Sagar, P. I. Mapp, P. Meesawatsom, L. Li, A. J. Bennett, D. A. Walsh, V. Chapman, The anti-NGF antibody muMab 911 both prevents and reverses pain behaviour and subchondral osteoclast numbers in a rat model of osteoarthritis pain. *Osteoarthritis Cartilage* **24**, 1587–1595 (2016).
67. M. V. Risbud, I. M. Shapiro, Role of cytokines in intervertebral disc degeneration: Pain and disc content. *Nat. Rev. Rheumatol.* **10**, 44–56 (2014).
68. Z. Hu, N. Deng, K. Liu, N. Zhou, Y. Sun, W. Zeng, CNTF-STAT3-IL-6 axis mediates neuroinflammatory cascade across Schwann cell-neuron-microglia. *Cell Rep.* **31**, 107657 (2020).
69. K. Vincent, S. Mohanty, R. Pinelli, R. Bonavita, P. Pricop, T. J. Albert, C. L. Dahia, Aging of mouse intervertebral disc and association with back pain. *Bone* **123**, 246–259 (2019).
70. M. Tajerian, J. D. Clark, The role of the extracellular matrix in chronic pain following injury. *Pain* **156**, 366–370 (2015).
71. Y. Kawasaki, Z.-Z. Xu, X. Wang, J. Y. Park, Z.-Y. Zhuang, P.-H. Tan, Y.-J. Gao, K. Roy, G. Corfas, E. H. Lo, R.-R. Ji, Distinct roles of matrix metalloproteases in the early- and late-phase development of neuropathic pain. *Nat. Med.* **14**, 331–336 (2008).
72. S. Wiese, M. Karus, A. Faissner, Astrocytes as a source for extracellular matrix molecules and cytokines. *Front. Pharmacol.* **3**, 120 (2012).
73. M. Xia, Y. Zhu, Fibronectin enhances spinal cord astrocyte proliferation by elevating P2Y1 receptor expression. *J. Neurosci. Res.* **92**, 1078–1090 (2014).
74. O. Airaksinen, J. I. Brox, C. Cedraschi, J. Hildebrandt, J. Klaber-Moffett, F. Kovacs, A. F. Mannion, S. Reis, J. B. Staal, H. Ursin, G. Zanoli, COST B13 Working Group on Guidelines for Chronic Low Back Pain, Chapter 4 European guidelines for the management of chronic nonspecific low back pain. *Eur. Spine J.* **15**, S192–S300 (2006).
75. K. Ren, R. Dubner, Interactions between the immune and nervous systems in pain. *Nat. Med.* **16**, 1267–1276 (2010).
76. M. Xu, E. W. Bradley, M. M. Weivoda, S. M. Hwang, T. Pirtskhalava, T. Decklever, G. L. Curran, M. Ogrodnik, D. Jurk, K. O. Johnson, V. Lowe, T. Tchkonia, J. J. Westendorf, J. L. Kirkland, Transplanted senescent cells induce an osteoarthritis-like condition in mice. *J. Gerontol. A Biol. Sci. Med. Sci.* **72**, 780–785 (2017).
77. J. N. Farr, M. Xu, M. M. Weivoda, D. G. Monroe, D. G. Fraser, J. L. Onken, B. A. Negley, J. G. Sfeir, M. B. Ogrodnik, C. M. Hachfeld, N. K. LeBrasseur, M. T. Drake, R. J. Pignolo, T. Pirtskhalava, T. Tchkonia, M. J. Oursler, J. L. Kirkland, S. Khosla, Targeting cellular senescence prevents age-related bone loss in mice. *Nat. Med.* **23**, 1072–1079 (2017).
78. J. E. Mayer, J. C. Iatridis, D. Chan, S. A. Qureshi, O. Gottesman, A. C. Hecht, Genetic polymorphisms associated with intervertebral disc degeneration. *Spine J.* **13**, 299–317 (2013).
79. D. J. Gorth, I. M. Shapiro, M. V. Risbud, A new understanding of the role of IL-1 in age-related intervertebral disc degeneration in a murine model. *J. Bone Miner. Res.* **34**, 1531–1542 (2019).
80. J. Virri, M. Grönblad, S. Seitsalo, A. Habtemariam, E. Kääpä, E. Karaharju, Comparison of the prevalence of inflammatory cells in subtypes of disc herniations and associations with straight leg raising. *Spine* **26**, 2311–2315 (2001).
81. Y. V. Teo, S. J. Hinthorn, A. E. Webb, N. Neretti, Single-cell transcriptomics of peripheral blood in the aging mouse. *Aging* **15**, 6–20 (2023).
82. A. Kavelaars, C. J. Heijnen, T cells as guardians of pain resolution. *Trends Mol. Med.* **27**, 302–313 (2021).
83. G. Laumet, J. Ma, A. J. Robison, S. Kumari, C. J. Heijnen, A. Kavelaars, T cells as an emerging target for chronic pain therapy. *Front. Mol. Neurosci.* **12**, 216 (2019).
84. I. Kaufmann, C. Eisner, P. Richter, V. Huge, A. Beyer, A. Chouker, G. Schelling, M. Thiel, Lymphocyte subsets and the role of Th1/Th2 balance in stressed chronic pain patients. *Neuroimmunomodulation* **14**, 272–280 (2007).
85. W. Raffaeli, V. Malafoglia, A. Bonci, M. Tenti, S. Ilari, P. Gremigni, C. Iannuccelli, C. Gioia, M. Di Franco, V. Mollace, L. Vitiello, C. Tomino, C. Muscoli, Identification of MOR-positive B

cell as possible innovative biomarker (Mu Lympho-Marker) for chronic pain diagnosis in patients with fibromyalgia and osteoarthritis diseases. *Int. J. Mol. Sci.* **21**, 1499 (2020).
86. M. J. Lacagnina, K. F. Willcox, N. Boukelmoune, C. J. Heijnen, P. M. Grace, B cells promote mechanical allodynia after peripheral nerve injury. *J. Pain* **24**, 37 (2023).
87. C. E. Moss, S. A. Johnston, J. V. Kimble, M. Clements, V. Codd, S. Hamby, A. H. Goodall, S. Deshmukh, I. Sudbery, D. Coca, H. L. Wilson, E. Kiss-Toth, Aging-related defects in macrophage function are driven by MYC and USF1 transcriptional programs. *Cell Rep.* **43**, 114073 (2024).
88. R. Domoto, F. Sekiguchi, M. Tsubota, A. Kawabata, Macrophage as a peripheral pain regulator. *Cells* **10**, 1881 (2021).
89. S. Krishnarajah, F. Ingelfinger, E. Friebel, D. Cansever, A. Amorim, M. Andreadou, D. Bamert, G. Litscher, M. Lutz, M. Mayoux, S. Mundt, F. Ridder, C. Sparano, S. A. Stifter, C. Ulutekin, S. Unger, M. Vermeer, P. Zwicky, M. Greter, S. Tugues, D. De Feo, B. Becher, Single-cell profiling of immune system alterations in lymphoid, barrier and solid tissues in aged mice. *Nat. Aging* **2**, 74–89 (2021).
90. K. Flurkey, J. M. Currer, D. E. Harrison, "Chapter 20 - Mouse models in aging research" in *The Mouse in Biomedical Research* (Academic Press, 2007), pp. 637–672.
91. V. Madhu, P. K. Boneski, E. Silagi, Y. Qiu, I. Kurland, A. R. Guntur, I. M. Shapiro, Hypoxic regulation of mitochondrial metabolism and mitophagy in nucleus pulposus cells is dependent on HIF-1α–BNIP3 axis. *J. Bone Miner. Res.* **35**, 1504–1524 (2020).
92. V. Madhu, M. Hernandez-Meadows, P. K. Boneski, Y. Qiu, A. R. Guntur, I. J. Kurland, R. A. Barve, M. V. Risbud, The mitophagy receptor BNIP3 is critical for the regulation of metabolic homeostasis and mitochondrial function in the nucleus pulposus cells of the intervertebral disc. *Autophagy* **19**, 1821–1843 (2023).
93. M. L. Bouxsein, S. K. Boyd, B. A. Christiansen, R. E. Guldberg, K. J. Jepsen, R. Müller, Guidelines for assessment of bone microstructure in rodents using micro-computed tomography. *J. Bone Miner. Res.* **25**, 1468–1486 (2010).
94. Y. Hao, S. Hao, E. Andersen-Nissen, W. M. Mauck, S. Zheng, A. Butler, M. J. Lee, A. J. Wilk, C. Darby, M. Zager, P. Hoffman, M. Stoeckius, E. Papalexi, E. P. Mimitou, J. Jain, A. Srivastava, T. Stuart, L. M. Fleming, B. Yeung, A. J. Rogers, J. M. McElrath, C. A. Blish, R. Gottardo, P. Smibert, R. Satija, Integrated analysis of multimodal single-cell data. *Cell* **184**, 3573–3587.e29 (2021).
95. S. Van Gassen, B. Callebaut, M. J. Van Helden, B. N. Lambrecht, P. Demeester, T. Dhaene, Y. Saeys, FlowSOM: Using self-organizing maps for visualization and interpretation of cytometry data. *Cytometry A* **87**, 636–645 (2015).
96. E. D. Amir, B. Lee, P. Badoual, M. Gordon, X. V. Guo, M. Merad, A. H. Rahman, Development of a comprehensive antibody staining database using a standardized analytics pipeline. *Front. Immunol.* **10**, (2019).
97. H. T. Maecker, J. P. McCoy, R. Nussenblatt, Standardizing immunophenotyping for the Human Immunology Project. *Nat. Rev. Immunol.* **12**, 191–200 (2012).
98. G. Finak, M. Langweiler, M. Jaimes, M. Malek, J. Taghiyar, Y. Korin, K. Raddassi, L. Devine, G. Obermoser, M. L. Pekalski, N. Pontikos, A. Diaz, S. Heck, F. Villanova, N. Terrazzini, F. Kern, Y. Qian, R. Stanton, K. Wang, A. Brandes, J. Ramey, N. Aghaeepour, T. Mosmann, R. H. Scheuermann, E. Reed, K. Palucka, V. Pascual, B. B. Blomberg, F. Nestle, R. B. Nussenblatt, R. R. Brinkman, R. Gottardo, H. Maecker, J. P. McCoy, Standardizing flow cytometry immunophenotyping analysis from the Human ImmunoPhenotyping Consortium. *Sci. Rep.* **6**, 20686 (2016).
99. R. Hefner, W. S. Torgerson, Theory and methods of scaling. New York: John Wiley and Sons, Inc., 1958. Pp. 460. *Behav. Sci.* **4**, 245–247 (2007).
100. M. D. Robinson, D. J. McCarthy, G. K. Smyth, edgeR: A Bioconductor package for differential expression analysis of digital gene expression data. *Bioinformatics* **26**, 139–140 (2010).
101. A. T. L. Lun, A. C. Richard, J. C. Marioni, Testing for differential abundance in mass cytometry data. *Nat. Methods* **14**, 707–709 (2017).
102. M. E. Ritchie, B. Phipson, D. Wu, Y. Hu, C. W. Law, W. Shi, G. K. Smyth, limma powers differential expression analyses for RNA-sequencing and microarray studies. *Nucleic Acids Res.* **43**, e47 (2015).
103. L. M. Weber, M. Nowicka, C. Soneson, M. D. Robinson, diffcyt: Differential discovery in high-dimensional cytometry via high-resolution clustering. *Commun. Biol.* **2**, 183 (2019).

Acknowledgments: We thank A. Kumar for assistance with tissue processing. **Funding:** This work was supported by the following: NIAMS grant R01AR055655 (to M.V.R.); NIAMS grant R01AR064733 (to M.V.R.); NIAMS grant R01AR074813 (to M.V.R.); University of Minho, Fundação para a Ciência e a Tecnologia (FCT) Ph.D. fellowship PD/BD/128077/2016 (to E.J.N.); NIAAA grant F31 AA030214 (to A.M.); NINDS grant R01NS079702 (to A.C.L.); and NINDS grant R01NS110385 (to A.C.L.). **Author contributions:** Conceptualization: E.J.N., O.K.O., E.V.B., V.M., P.R., A.S.D., M.D.S., A.C.L., and M.V.R. Data curation: E.J.N., P.R., M.D.S., A.C.L., and M.V.R. Formal analysis: E.J.N., O.K.O., E.V.B., V.M., V.A.T., P.R., M.D.S., A.M., and A.C.L. Funding acquisition: A.C.L. and M.V.R. Investigation: E.J.N., O.K.O., E.V.B., V.M., V.A.T., P.R., A.S.D., M.D.S., and A.C.L. Methodology: E.J.N., O.K.O., E.V.B., V.M., V.A.T., A.S.D., M.D.S., A.C.L., and M.V.R. Project administration: E.J.N., M.D.S., A.C.L., and M.V.R. Resources: E.J.N., M.D.S., A.C.L., and M.V.R. Software: O.K.O., M.D.S., and A.M. Supervision: E.J.N., A.S.D., M.D.S., A.C.L., and M.V.R. Validation: E.J.N., O.K.O., E.V.B., V.M., V.A.T., P.R., M.D.S., and A.C.L. Visualization: E.J.N., O.K.O., E.V.B., V.A.T., P.R., A.S.D., M.D.S., and A.C.L. Writing—original draft: E.J.N., O.K.O., A.S.D., M.D.S., A.C.L., and M.V.R. Writing—review and editing: E.J.N., O.K.O., P.R., A.C.L., and M.V.R. **Competing interests:** The authors declare that they have no competing interests. **Data and materials availability:** All data needed to evaluate the conclusions in the paper are present in the paper and/or the Supplementary Materials. The microarray and scRNA-seq datasets that support the findings of this study are openly available in the GEO database at GSE252383 and GSE252474, respectively. Relevant R scripts can be found at https://github.com/mrisbudlab or https://datadryad.org/stash/share/UlzO6e_x3uLqiw3zPr0Zv0ntHbXZPrXP-hG02aA5Iec.

Submitted 20 February 2024
Accepted 19 March 2025
Published 23 April 2025
10.1126/sciadv.ado6847